Nuclear translocation of AMPK-α1 potentiates striatal neurodegeneration in Huntington's disease

Tz-Chuen Ju,[1,3] Hui-Mei Chen,[3] Jiun-Tsai Lin,[3] Ching-Pang Chang,[3] Wei-Cheng Chang,[1] Jheng-Jie Kang,[1] Cheng-Pu Sun,[2] Mi-Hua Tao,[3] Pang-Hsien Tu,[3] Chen Chang,[3] Dennis W. Dickson,[4] and Yijuang Chern[1,3]

[1]Institute of Neuroscience and [2]Institute of Biochemistry and Molecular Biology, School of Life Sciences, National Yang Ming University, Taipei 112, Taiwan
[3]Division of Neuroscience, Institute of Biomedical Sciences, Academia Sinica, Taipei 11529, Taiwan
[4]Department of Neuroscience, Mayo Clinic College of Medicine, Jacksonville, FL 32224

Adenosine monophosphate–activated protein kinase (AMPK) is a major energy sensor that maintains cellular energy homeostasis. Huntington's disease (HD) is a neurodegenerative disorder caused by the expansion of CAG repeats in the *huntingtin* (*Htt*) gene. In this paper, we report that activation of the α1 isoform of AMPK (AMPK-α1) occurred in striatal neurons of humans and mice with HD. Overactivation of AMPK in the striatum caused brain atrophy, facilitated neuronal loss, and increased formation of Htt aggregates in a transgenic mouse model (R6/2) of HD. Such nuclear accumulation of AMPK-α1 was activity dependent. Prevention of nuclear translocation or inactivation of AMPK-α1 ameliorated cell death and down-regulation of Bcl2 caused by mutant Htt (mHtt). Conversely, enhanced expression of Bcl2 protected striatal cells from the toxicity evoked by mHtt and AMPK overactivation. These data demonstrate that aberrant activation of AMPK-α1 in the nuclei of striatal cells represents a new toxic pathway induced by mHtt.

Introduction

Huntington's disease (HD) is an autosomal dominant neurodegenerative disease that manifests clinically as progressive involuntary movement disorders, dementia, and eventual death (Martin and Gusella, 1986). It is caused by CAG trinucleotide expansion in exon 1 of the *huntingtin* (*Htt*) gene. When the number of CAG repeats exceeds 36, the translated polyglutamine (polyQ) containing the Htt protein (mutant Htt [mHtt]) interferes with the normal functions of many cellular proteins and subsequently jeopardizes important cellular machinery (The Huntington's Disease Collaborative Research Group, 1993; Landles and Bates, 2004; Buckley et al., 2010). Severe tissue damage is observed in the neostriatum, nigrostriatal tract, and cortex (Estrada Sánchez et al., 2008).

In addition to neuronal dysregulation, metabolic abnormalities are another important hallmark of HD (Pratley et al., 2000).

Hyperglycemia and abnormal glucose metabolism were observed in several mouse models of HD and in patients with HD (Hurlbert et al., 1999). Deficiencies in several other metabolic pathways (e.g., cholesterol biosynthesis and urea cycle metabolism) are also well documented (Chiang et al., 2007; Valenza et al., 2007). AMP-activated protein kinase (AMPK) is a major energy sensor that regulates an array of downstream target genes and maintains cellular energy homeostasis by activating energy production and inhibiting energy expenditure in many different tissues (Long and Zierath, 2006). AMPK comprises three subunits (α, β, and γ) and can be activated by several upstream kinases (CaM-dependent protein kinase kinase [CaMKK] and LKB1) via the phosphorylation of its Thr residue 172 within the catalytic domain of the α subunit (Stein et al., 2000). Other kinases (including the cAMP-dependent kinase [PKA] and Ca^{2+}/CaM-dependent protein kinase II [CaMKII]) were also shown to regulate the activity of AMPK (Hurley et al., 2006; Raney and Turcotte, 2008). The α subunit of AMPK is the catalytic subunit and has at least two different isoforms (α1 and α2). AMPK-α1 is predominantly expressed in the cytoplasm, whereas the

Correspondence to Yijuang Chern: bmychern@ibms.sinica.edu.tw

Abbreviations used in this paper: AAV, adeno-associated virus; AD, Alzheimer's disease; AICAR, aminoimidazole carboxamide riboside; AMPK, AMP-activated protein kinase; CC, compound C; CREB, cAMP response element binding; CSC, 8-[-3-chlorostyryl]-caffeine; GAPDH, glyceraldehyde-3-phosphate dehydrogenase; HD, Huntington's disease; hrGFP, humanized *Renilla* GFP; Htt, Huntingtin; mHtt, mutant Htt; MRI, magnetic resonance imaging; NES, nuclear export signal; NeuN, neuronal nuclei; PARP, poly (ADP-ribose) polymerase; PB, phosphate buffer; polyQ, polyglutamine; qPCR, quantitative PCR; RIPA, radioimmunoprecipitation assay; VBR, ventricle to brain ratio; WT, wild type.

A The caudate nucleus

Non-HD-1 — AMPK α-p | Hoechst | Merge 31% ± 3
HD patient-1 — AMPK α-p | Hoechst | Merge 71% ± 5

Non-HD-1 — AMPK-α1 | Hoechst | Merge 22% ± 5
HD patient-1 — AMPK-α1 | Hoechst | Merge 77% ± 4

B The frontal cortex

Non-HD-1 — AMPK α-p | Hoechst | Merge 22% ± 5
HD patient-1 — AMPK α-p | Hoechst | Merge 67% ± 8

Non-HD-1 — AMPK-α1 | Hoechst | Merge 20% ± 7
HD patient-1 — AMPK-α1 | Hoechst | Merge 85% ± 4

C

WT — AMPK α-p | Hoechst | Merge 18% ± 2
R6/2 — AMPK α-p | Hoechst | Merge 83% ± 5

D

WT — AMPK α1 | Hoechst | Merge 19% ± 4
R6/2 — AMPK α1 | Hoechst | Merge 88% ± 5

E

IP: α1 | NRS
Input | IP
WT R6/2 | WT R6/2 | WT R6/2 striatum
AMPK α-p
AMPK α1

F

IP: α2 | NRS
Input | IP
WT R6/2 | WT R6/2 | WT R6/2 striatum
AMPK α-p
AMPK α2

G

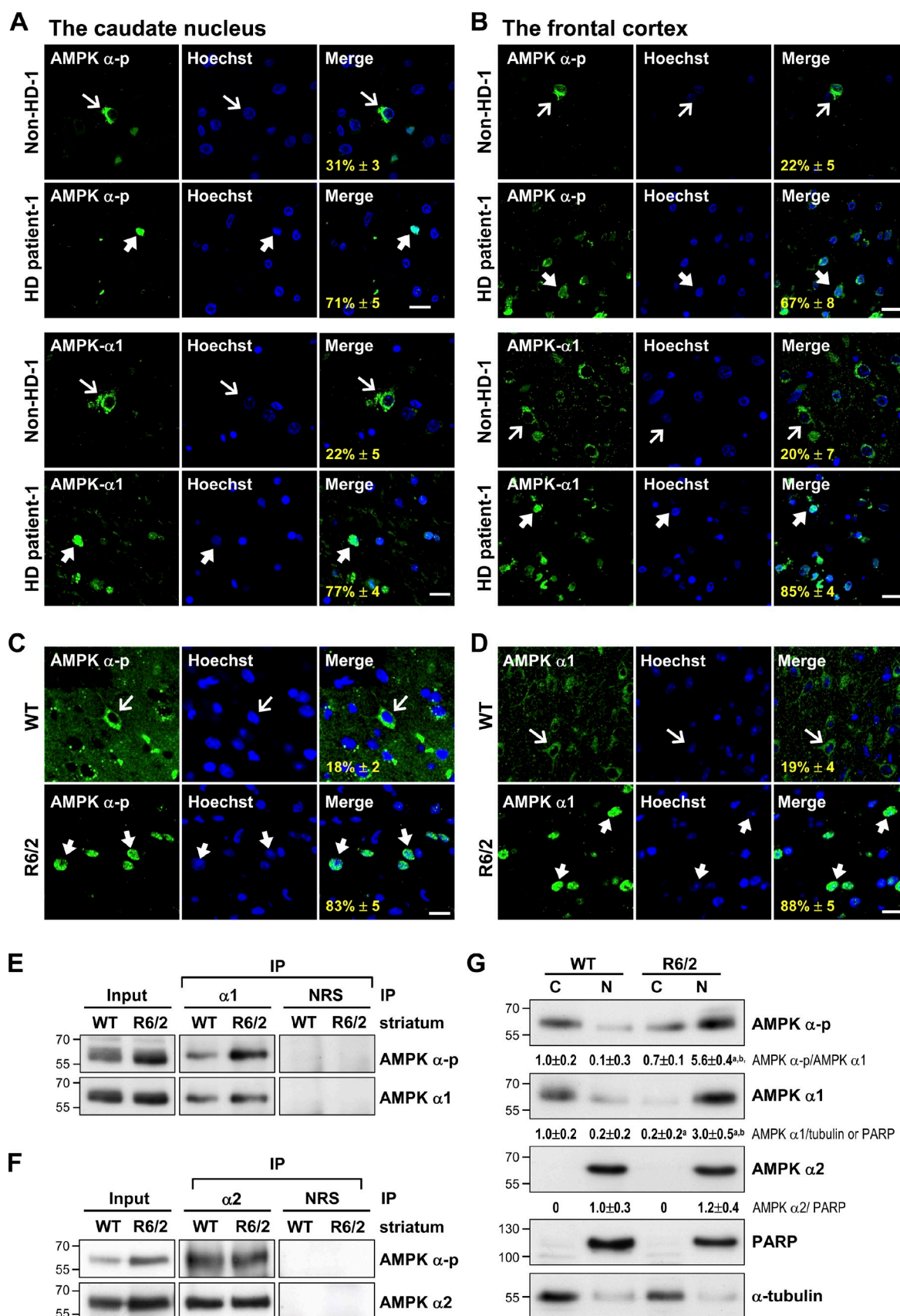|	WT		R6/2	
	C	N	C	N
AMPK α-p				
AMPK α-p/AMPK α1	1.0±0.2	0.1±0.3	0.7±0.1	5.6±0.4[a,b,]
AMPK α1				
AMPK α1/tubulin or PARP	1.0±0.2	0.2±0.2	0.2±0.2[a]	3.0±0.5[a,b]
AMPK α2				
AMPK α2/ PARP	0	1.0±0.3	0	1.2±0.4
PARP				
α-tubulin				

Figure 1. **Selective activation and nuclear enrichment of AMPK-α1 in striatal neurons of patients and mice with HD.** (A and B) The caudate nucleus (A) and frontal cortex (B) of HD patients and age-matched controls were analyzed. Immunofluorescence staining of AMPK-α-p (green) or AMPK-α1 (green) was conducted. (C and D) Immunofluorescence staining of AMPK-α-p (C, green) or AMPK-α1 (D, green) was conducted in brains of 12-wk-old mice. Nuclei were

α2 subunit is located mainly in the nucleus (Salt et al., 1998; Turnley et al., 1999). Localization of AMPK is sensitive to various stresses, including heat shock, energy depletion, and oxidants (Kodiha et al., 2007). In the nucleus, AMPK phosphorylates several transcription factors and cofactors (including FOXO3, peroxisome proliferator-activated receptor γ coactivator 1α [PGC-1α], p300, and p53) and regulates gene expression (Yang et al., 2001; Greer et al., 2007; Jäger et al., 2007; Okoshi et al., 2008; Chaturvedi et al., 2009). The mechanism responsible for the nuclear–cytoplasmic shuttling of AMPK is largely known.

The function and regulation of AMPK and its role in neurodegenerative diseases have attracted much attention. For example, higher activities of AMPK were found in neurons with ischemia, HD, and Alzheimer's disease (AD; Chou et al., 2005; McCullough et al., 2005; Lopez-Lopez et al., 2007). The underlying mechanisms and consequences of AMPK activation in neurodegenerative disorders remain mostly uncharacterized. The substrates of AMPK include proteins involved in energy metabolism and other cellular mechanisms such as apoptosis and cellular responses to oxidative stress (Tsuboi et al., 2003; Cai et al., 2007). We previously demonstrated that AMPK is abnormally activated in the striatum of a transgenic mouse model of HD (R6/2; Chou et al., 2005). In the present study, we demonstrate that activation of AMPK-α1 in striatal neurons is closely associated with mHtt-induced cell death. This AMPK-mediated neurotoxicity requires the nuclear translocation of AMPK-α1 to suppress the expression of *Bcl2*. Most importantly, a beneficial reagent (CGS21680 [CGS]; Chou et al., 2005) protected striatal cells from the mHtt-mediated toxicity via (at least partially) interfering with the detrimental action of AMPK-α1.

Results

Selective activation and nuclear enrichment of AMPK-α1 in striatal neurons of humans and mice with HD

To characterize the role of AMPK in HD pathogenesis, we first evaluated the activation and subcellular localization of AMPK in brains of HD patients using an immunofluorescence staining technique. Surprisingly, nuclear accumulations of activated AMPK (i.e., the AMPK that is phosphorylated at Thr^{172}, AMPK-α-p) were observed in the caudate nucleus (Fig. 1 A) and frontal cortex (Figs. 1 B and S1 A) of both male and female patients with HD. In contrast, activated AMPK appeared in the cytoplasm of cells in brains of non-HD subjects (Figs. 1 [A and B] and S1 [B and C] and Table I). Similar nuclear enrichment of AMPK-α-p was also observed in the striatum of a transgenic mouse model of HD, whereas most AMPK-α-p appeared in the cytoplasm of striatal cells in wild-type (WT) mice (Fig. 1 C).

To verify whether mHtt directly regulates AMPK in striatal cells, the activation of AMPK in the presence of mHtt was evaluated in three striatal cell lines. The level of AMPK-α-p was higher in ST*Hdh^{Q109}* cells, which carry the polyQ-expanded mouse gene *Htt*, than in the control cell line (ST*Hdh^{Q7}*), which encodes seven CAG repeats in the *Htt* gene (Fig. 2 A). Similarly, the transient expression of Htt-(Q)$_{109}$–humanized *Renilla* GFP (hrGFP; 109Q) in ST14A cells caused a higher level of AMPK phosphorylation than did the expression of Htt-(Q)$_{25}$-hrGFP (25Q; Fig. 2 B). A similar result of activated AMPK-α was also observed in the striatum of both male and female R6/2 mice (Figs. 2 C and S1 D). Moreover, AMPK activation and nuclear location of AMPK-α1 in the brain of mice and patients with HD showed no gender differences (Figs. 1 [A and B] and S1 [A–D]).

Next, we performed experiments to identify the entity in the AMPK-α subunit that is regulated by mHtt. Immunoprecipitation of AMPK-α1 revealed that the phosphorylation of AMPK-α1 at Thr^{172} was significant in the striatum of R6/2 mice, whereas it was barely detectable in that of WT mice (Fig. 1 E). No change in the phosphorylation status of AMPK-α2 at Thr^{172} was detected in the striatum of either WT or R6/2 mice (Fig. 1 F). Consistent with these findings, Western blot analyses of fractionated striatal proteins harvested from 12-wk-old WT and R6/2 mice showed that AMPK-α1 and AMPK-α-p were largely located in the striatal nucleus and cytoplasm of R6/2 and WT mice, respectively (Fig. 1 G). In contrast, AMPK-α2 mainly existed in nuclei of striatal cells of both R6/2 and WT mice (Fig. 1 G), further suggesting that AMPK-α2 did not contribute to the nuclear enrichment of AMPK-α-p in the striatum of R6/2 mice. Moreover, down-regulation of AMPK-α1 using a small hairpin RNA (α1-shRNA) in ST*Hdh^{Q109}* cells markedly reduced the level of activated AMPK (AMPK-α-p; Fig. 2 D), further supporting the idea that AMPK-α1 is the major phosphorylated AMPK isoform in striatal cells expressing mHtt. These data show that the expression of mHtt selectively activates and causes the nuclear enrichment of AMPK-α1.

Activation of AMPK-α1 compromises the survival of striatal neurons

The role of AMPK in striatal cells was first examined by a daily i.p. injection of 400 mg/kg aminoimidazole carboxamide riboside (AICAR) or vehicle into WT and R6/2 mice for 5 wk from the age of 7 wk. A major characteristic of HD is the enlargement of the ventricles, which is accompanied by a progressive reduction in the brain weight. An in vivo 3D magnetic resonance imaging (MRI) analysis revealed a higher ventricle to brain ratio (VBR) in R6/2 mice than in WT mice (Fig. 3, A and B). A histological examination and Nissl staining revealed that the

stained with Hoechst (blue). The numbers shown in the bottom left corners of the merged images are the percentages of cells expressing nuclear AMPK-α-p or AMPK-α1. Thin arrows mark cells containing AMPK, which are located mostly in cytoplasmic regions. Thick arrows mark cells with nuclei enriched with AMPK. Values represent the mean ± SEM of at least three independent experiments. At least 200 cells from each sample were analyzed. Bars, 20 μm. (E and F) Total striatal lysate of 12-wk-old mice was immunoprecipitated (IP) using the indicated antibody and subjected to Western blot analyses. (G) The cytoplasmic (C) and nuclear (N) fractions were harvested from the striatum of 12-wk-old mice and assessed using Western blot analysis. PARP and α-tubulin were respective markers for the nuclear and cytoplasmic fractions. Data are presented as the mean ± SEM of three independent experiments. Molecular mass is indicated in kilodaltons. a, $P < 0.05$ versus WT cytoplasmic; b, $P < 0.05$ versus WT nuclear. NRS, normal rabbit serum.

Table I. **Summary of demographic data, neuropathology, and experimental results of human subjects**

Case	PMI	Brain area	Nuclear localization of AMPK-α-p	Nuclear localization of AMPK-α1	Age	Gender	HD Vonsattel grade	Other pathology
	h		%	%	yr			
HD-1[a]	9	Caudate nucleus	71 ± 5	77 ± 4	80	F	I	Cortical amyloid plaques
HD-2[a]	<24	Caudate nucleus	67 ± 7	75 ± 5	70	F	IV	Brainstem Lewy body
HD-1[a]	9	Frontal cortex	67 ± 8	85 ± 4	80	F	I	Cortical amyloid plaques
HD-2[a]	<24	Frontal cortex	69 ± 6	70 ± 9	70	F	IV	Brainstem Lewy body
HD-3[b]	15	Frontal cortex	51 ± 8	56 ± 4	57	M	I	None
HD-4[b]	17	Frontal cortex	60 ± 4	64 ± 7	58	M	I	None
Non–HD-1[a]	6	Caudate nucleus	31 ± 7	22 ± 5	93	M	n.a.	AD break NFT
Non–HD-2[a]	14	Caudate nucleus	17 ± 5	20 ± 6	88	F	n.a.	None
Non–HD-3[a]	<24	Caudate nucleus	24 ± 6	31 ± 3	82	F	n.a.	None
Non–HD-4[a]	12	Caudate nucleus	25 ± 5	18 ± 5	78	M	n.a.	AD break NFT
Non–HD-5[a]	<24	Caudate nucleus	18 ± 4	26 ± 3	74	M	n.a.	None
Non–HD-6[a]	<24	Caudate nucleus	21 ± 5	22 ± 3	83	M	n.a.	None
Non–HD-1[a]	6	Frontal cortex	22 ± 5	20 ± 7	93	M	n.a.	AD break NFT
Non–HD-2[a]	14	Frontal cortex	12 ± 4	18 ± 6	88	F	n.a.	None
Non–HD-3[a]	<24	Frontal cortex	19 ± 7	22 ± 8	82	F	n.a.	None
Non–HD-4[a]	12	Frontal cortex	27 ± 4	21 ± 5	78	M	n.a.	AD break NFT
Non–HD-5[a]	<24	Frontal cortex	25 ± 3	21 ± 7	74	M	n.a.	None
Non–HD-6[a]	<24	Frontal cortex	22 ± 5	17 ± 4	83	M	n.a.	None

Significant amounts of phosphorylated AMPK-α at Thr^{172} (AMPK-α-p) and AMPK-α1 were found in nuclei in brains of HD patients but not in those of age-matched controls. Brain sections were analyzed by immunofluorescence staining of AMPK-α-p or AMPK-α1 as shown in Fig. 1 and Fig. S1. At least 200 cells were counted in brain sections of each subject. The Alzheimer-type pathology (both senile plaques and neurofibrillary tangles [NFTs]) was assessed by thioflavin-S fluorescence microscopy. The Braak neurofibrillary tangle stage was assigned based on the counts of plaques and neurofibrillary tangles with this method. F, female; M, male; n.a., not applicable; PMI, postmortem interval.

[a]Cases obtained from the Mayo Clinic College of Medicine, Rochester, MN.

[b]Cases obtained from the National Institute of Child Health and Development Brain and Tissue Bank for Developmental Disorders at the University of Maryland, College Park, MD.

aforementioned brain atrophy observed in 12-wk-old R6/2 mice probably resulted from a reduction in the size of the neurons (Fig. 3, D and E). Importantly, chronic treatment with AICAR further increased the VBR of R6/2 mice (Fig. 3, A and B). Consistent with these findings, AICAR also reduced the brain weight of R6/2 mice (Fig. 3 C). The number of neurons in the striatum was also markedly lower in AICAR-treated R6/2 mice than in control R6/2 mice (Fig. 3, D and F). In both WT and R6/2 mice, the level of AMPK-α-p was elevated in the striatum of mice chronically treated with AICAR (Fig. 3 G). Activation of caspase 3 and reduced expression of Bcl2 were also observed in the striatum of AICAR-treated mice (Fig. 3, H and I, respectively), suggesting a detrimental effect of activated AMPK on the striatum. Filter retardation assays revealed that the activation of AMPK by AICAR markedly enhanced the formation of mHtt aggregates in R6/2 mice (Fig. 3 J). To ensure that the detrimental effect of AICAR was caused by direct activation of AMPK in the brain, we directly infused AICAR (3 µg/animal/day; Florant et al., 2010) into the striatum of WT and R6/2 mice for 7 d using ALZET osmotic pumps at the age of 12 wk. As expected, AICAR enhanced the level of AMPK-α-p and the nuclear localization of AMPK-α1 in the striatum of both WT and R6/2 mice (Figs. 4 A and S2). Conversely, an AMPK inhibitor, compound C (CC), greatly reduced the nuclear localization of AMPK-α1 in R6/2 mice (Fig. S2). Next, we assessed neuronal toxicity using SR-FLIVO, a red fluorescent probe that forms covalent bonds with active caspases and therefore detects apoptotic cells in vivo (Escribano et al., 2009). As shown in Fig. 4 B,

signals of activated caspases were detected in the striatum of R6/2 but not WT mice. Moreover, the number of neurons in the striatum of R6/2 mice was significantly reduced by AICAR (Fig. 4, C and E). Consistent with the aforementioned detrimental effect of the intrastriatal infusion of AICAR, stimulation of AMPK with AICAR also worsened the rotarod performance and reduced the life span of R6/2 mice (Fig. 4, F and G). Collectively, these findings show that AMPK potentiates the striatal neurodegeneration triggered by mHtt.

Similar detrimental roles of AMPK were also observed in striatal cell lines. We found that the stimulation of AMPK with AICAR caused dose-dependent cell death in STHdh^{Q7} and STHdh^{Q109} cells (Fig. 5, A and B). STHdh^{Q109} cells, which had greater AMPK activity, were more sensitive to AICAR-induced cell death than were STHdh^{Q7} cells, as assessed by flow cytometry (Fig. 5 A) and the 3-(4,5-dimethylthiazol-2-yl)-2,5-diphenyltetrazolium bromide (MTT) reduction assay (Fig. 5 B). Moreover, an inhibitor of AMPK, CC, markedly increased cell survival after AMPK activation (Fig. 5 C). Consistent with the aforementioned observations made in striatal neurons of R6/2 mice, activated AMPK and AMPK-α1 predominantly appeared in the cytoplasm and nuclei of STHdh^{Q7} and STHdh^{Q109} cells, respectively (Fig. 5, D and E). Because stimulation of AMPK with AICAR significantly enhanced the nuclear localization of AMPK-α-p and AMPK-α1 in striatal cells, whereas blocking AMPK using CC eliminated the nuclear accumulation of AMPK-α1 in the presence of mHtt (Figs. 4 A, 5 D, and S2), we reasoned that activation of AMPK-α1 might promote its
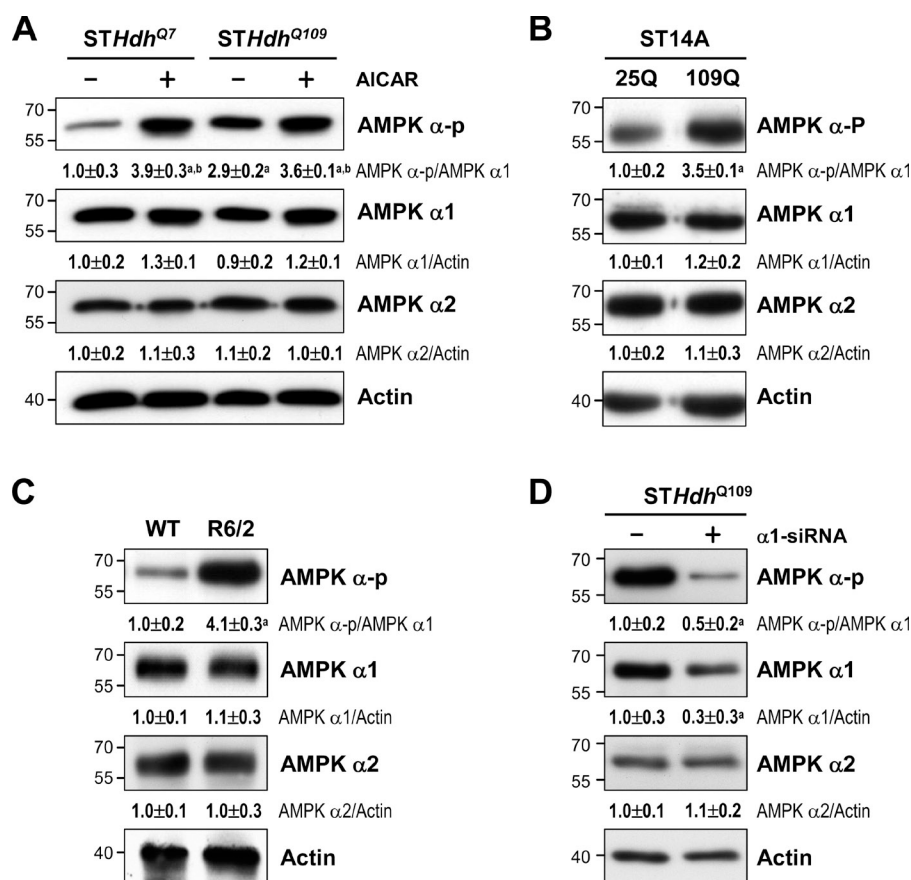
A

	ST*Hdh*^Q7		ST*Hdh*^Q109	
	−	+	−	+	AICAR

nuclear translocation. In line with this hypothesis, an exogenously expressed dominant-positive AMPK-α1 mutant (AMPK-α1-T172D) was detected consistently in the nuclei of ST*Hdh*^Q7 cells, whereas a dominant-negative AMPK-α1 mutant (AMPK-α1-T172A) appeared in the cytoplasm (Fig. S3 B). Collectively, these results suggest that mHtt causes the phosphorylation and activation of AMPK-α1, which is then translocated into the nuclei.

To assess whether the nuclear localization of AMPK-α1 is important, we created AMPK-α1 variants to which were fused an NLS or a nuclear export signal (NES). The inclusion of an NLS or NES restricted the location of the corresponding AMPK-α1 mutant to nuclei or the cytoplasm, respectively (Fig. S3 C). The expression of AMPK-α1-T172D-NLS, but not AMPK-α1-T172D-NES, significantly caused cell death in ST*Hdh*^Q109 cells (Fig. 5, F and G). To determine whether nuclear localization of AMPK-α1 facilitates striatal neurodegeneration in HD, we created adeno-associated viruses (AAVs) carrying AMPK-α1 variants fused to the YFP. Fusion of AMPK-α1 variants with YFP or V5 did not affect their functions or distributions (Fig. S3 A). An intrastriatal injection of AAV-AMPK-α1-T172D-NLS, but not AAV-AMPK-α1-T172D-NES or AAV-GFP (a control virus), for 5 wk from the age of 7 wk enhanced the number of apoptotic cells that contained active caspases in the striatum of R6/2 mice compared with those in WT mice (Fig. 6, A and C). We identified infected striatal cells by the expression of YFP. The number of AMPK-α1-T172D-NLS–positive neurons in the striatum of R6/2 mice was lower than that of AMPK-α1-T172D-NES– and

GFP-positive neurons (Fig. 6 D), suggesting that the nuclear localization of AMPK-α1 is critical for the degeneration of striatal neurons in the presence of mHtt.

Because Ca^{2+} signaling is disrupted in striatal neurons of HD mice (Tang et al., 2005) and because Ca^{2+}/CaM-dependent protein kinases (including CaMKK and CaMKII) were reported to be upstream of AMPK (Anderson et al., 2008), we evaluated whether CaMKK and CaMKII were involved in the activation of AMPK-α1 by mHtt. As shown in Fig. 7 A, treatment of ST*Hdh*^Q109 cells with an inhibitor (KN62) of CaMKII significantly reduced AMPK activation as assessed by the level of AMPK-α-p. Most importantly, KN62 blocked the nuclear enrichment of AMPK-α1 (Fig. 7 B). A CaMKK inhibitor (STO-609) at up to 10 μM, in contrast, did not prevent the nuclear enrichment of AMPK-α1 in ST*Hdh*^Q109 cells (unpublished data). Consistent with the importance of CaMKII in the activation of AMPK-α1 by mHtt, we found that the activity of CaMKII in ST*Hdh*^Q109 cells was higher than that in ST*Hdh*^Q7 cells as assessed by the phosphorylation level of CaMKII at Thr^{286} (CaMKII-pT286; Swulius and Waxham, 2008), an autophosphorylation site by CaMKII (Fig. 7 C). Similarly, the activity of CaMKII in the striatum of R6/2 mice was significantly higher than that of WT mice (Fig. 7 D). An intrastriatal injection of KN62 (10 μg per mouse) markedly reduced the level of nuclear AMPK-α-p and AMPK-α1 in the striatum of R6/2 mice (Fig. 7, E–G). Collectively, these findings suggest that the dysregulated CaMKII might mediate the abnormal activation of AMPK-α1 by mHtt.
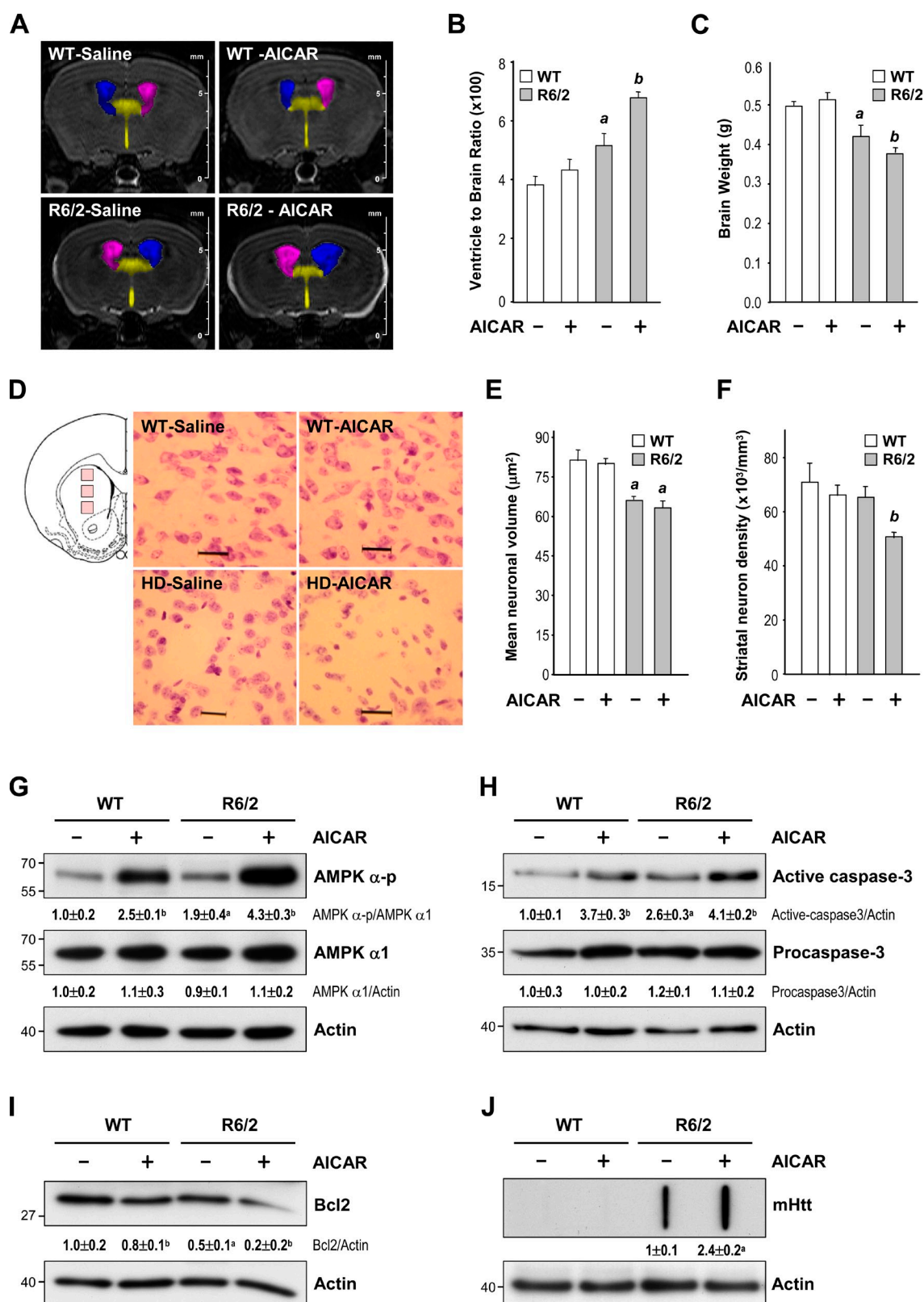
A

WT-Saline   WT -AICAR

R6/2-Saline   R6/2 - AICAR

B

Ventricle to Brain Ratio (x100)

□ WT
▨ R6/2

AICAR − + − +

C

Brain Weight (g)

□ WT
▨ R6/2

AICAR − + − +

D

WT-Saline   WT-AICAR

HD-Saline   HD-AICAR

E

Mean neuronal volume (μm²)

□ WT
▨ R6/2

AICAR − + − +

F

Striatal neuron density (x10³/mm³)

□ WT
▨ R6/2

AICAR − + − +

G

	WT		R6/2		
	−	+	−	+	AICAR
70 — 55 —					AMPK α-p
	1.0±0.2	2.5±0.1[b]	1.9±0.4[a]	4.3±0.3[b]	AMPK α-p/AMPK α1
70 — 55 —					AMPK α1
	1.0±0.2	1.1±0.3	0.9±0.1	1.1±0.2	AMPK α1/Actin
40 —					Actin

H

	WT		R6/2		
	−	+	−	+	AICAR
15 —					Active caspase-3
	1.0±0.1	3.7±0.3[b]	2.6±0.3[a]	4.1±0.2[b]	Active-caspase3/Actin
35 —					Procaspase-3
	1.0±0.3	1.0±0.2	1.2±0.1	1.1±0.2	Procaspase3/Actin
40 —					Actin

I

	WT		R6/2		
	−	+	−	+	AICAR
27 —					Bcl2
	1.0±0.2	0.8±0.1[b]	0.5±0.1[a]	0.2±0.2[b]	Bcl2/Actin
40 —					Actin

J

	WT		R6/2		
	−	+	−	+	AICAR
					mHtt
			1±0.1	2.4±0.2[a]	
40 —					Actin

Figure 3. **Activation of AMPK enhances brain atrophy, neuronal loss, and aggregate formation in the striatum of R6/2 mice.** (A–J) Mice were treated daily with AICAR (400 mg/kg of body weight, i.p.) or saline for 5 wk from the age of 7 wk. (A) Representative 3D brain images from vehicle-treated WT mice ($n = 6$), saline-treated R6/2 mice ($n = 6$), AICAR-treated WT mice ($n = 6$), and AICAR-treated R6/2 mice ($n = 7$). (B and C) The VBR values (B) and brain weights (C) are illustrated. a, $P < 0.05$ between saline-treated WT and R6/2 mice; b, $P < 0.05$ versus saline-treated mice. (D) Brain sections of 12-wk-old mice (saline-treated WT mice [$n = 3$], saline-treated R6/2 mice [$n = 6$], AICAR-treated WT mice [$n = 5$], and AICAR-treated R6/ 2 mice [$n = 6$]) were stained with Nissl stain. Three pictures (marked by pink boxes) were taken from each striatal section and are illustrated on the left. Bars, 25 μm. (E and F) The histograms show the striatal neuronal area (E) and the number of striatal neurons (F). a, $P < 0.05$ between untreated WT and R6/2 mice; b, $P < 0.05$ versus
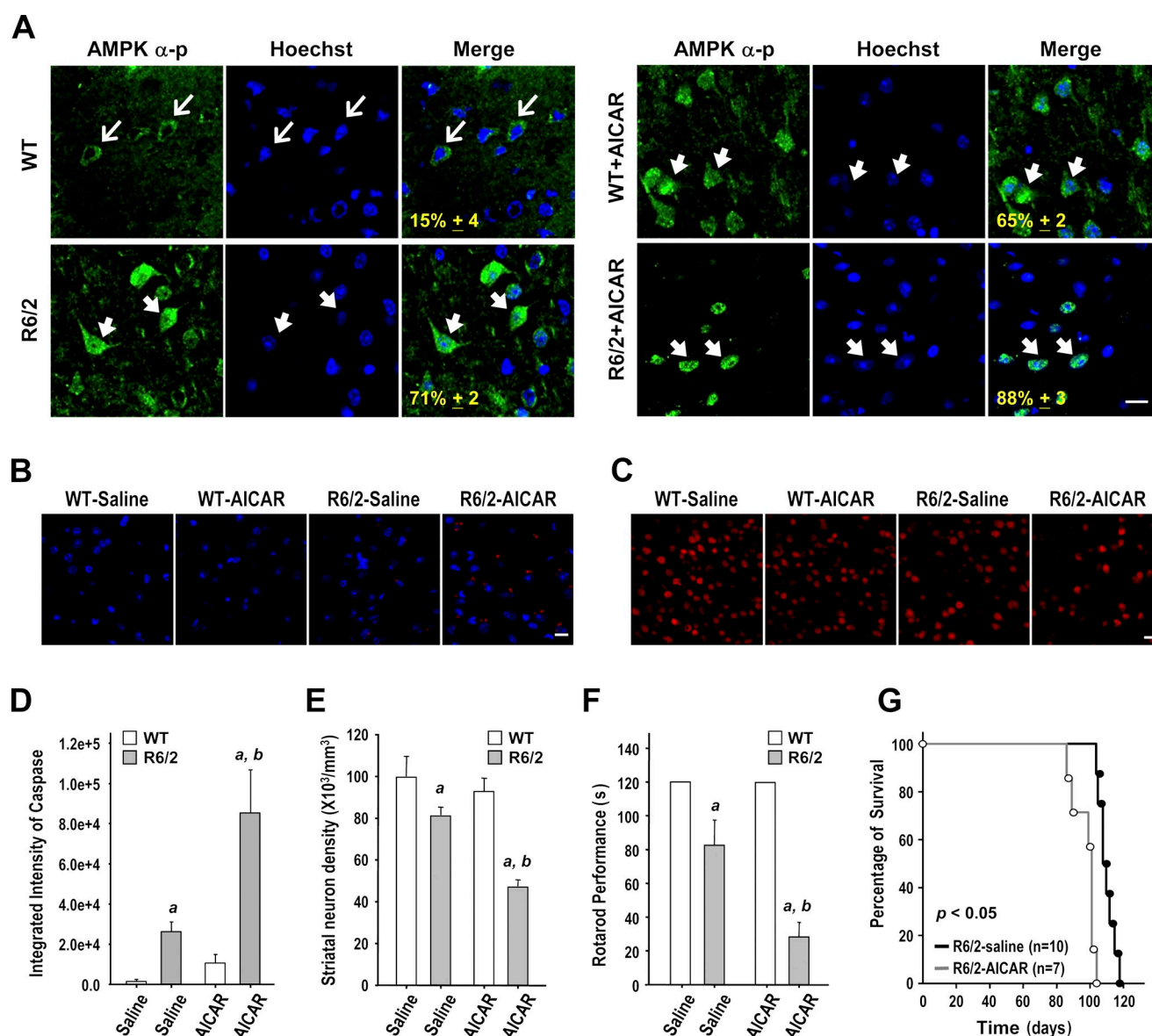
Figure 4. **Activation of AMPK enhances neuronal loss and motor dysfunction in R6/2 mice.** (A–C) 12-wk-old mice were infused with AICAR (3 μg/animal/day) or saline via osmotic minipumps for 7 d and then subjected to immunohistochemical analyses. Expressions of AMPK-α-p (A, green), active caspases (B, red), and NeuN (C, red) in the striatum of the indicated animals ($n = \sim 3$–6 for each condition) are shown. Nuclei were stained with Hoechst (A and B, blue). The numbers shown in the bottom left corners of the merged images are the percentages of cells expressing nuclear AMPK-α-p (A). Thin arrows mark cells expressing AMPK-α-p, which is mostly located in cytoplasmic regions. Thick arrows mark cells with nuclei enriched with AMPK-α-p. Bars, 20 μm. (D and E) The histograms show the integrated intensity of active caspases (D) and the number of striatal neurons (E). At least 200 and 1,000 cells from each animal were respectively counted and measured to determine the nuclear enrichment of AMPK-p–positive neurons and the number of neurons in the striatum, respectively. (F) Rotarod performance ($n = 10$ for each condition) was determined. (E and F) Data are presented as the mean ± SEM. a, $P < 0.05$ between WT and R6/2 mice; b, $P < 0.05$ versus R6/2-saline mice. (G) Survival was assessed by a Kaplan–Meier survival analysis.

untreated mice. Nine frames from three brain sections spaced evenly throughout the striatum were analyzed for each animal by an investigator blind to the experimental condition. At least 500 and 700 cells from each animal were respectively counted and measured to determine the size of neurons and the number of neurons in the striatum. (B, C, E, and F) Data are presented as the mean ± SEM. (G–I) Striatal lysates were analyzed by Western blot analyses. Results were normalized to those of actin. a, $P < 0.05$ between untreated WT and R6/2 mice; b, $P < 0.05$ versus saline-treated mice. (J) The amount of mHtt aggregates in striatal lysates was analyzed by a filter retardation assay. Insoluble aggregates retained on the filters were detected using an anti-Htt antibody. a, $P < 0.05$ versus saline-treated R6/2 mice. (G–J) Data are presented as the mean ± SEM of three independent experiments. Molecular mass is indicated in kilodaltons.
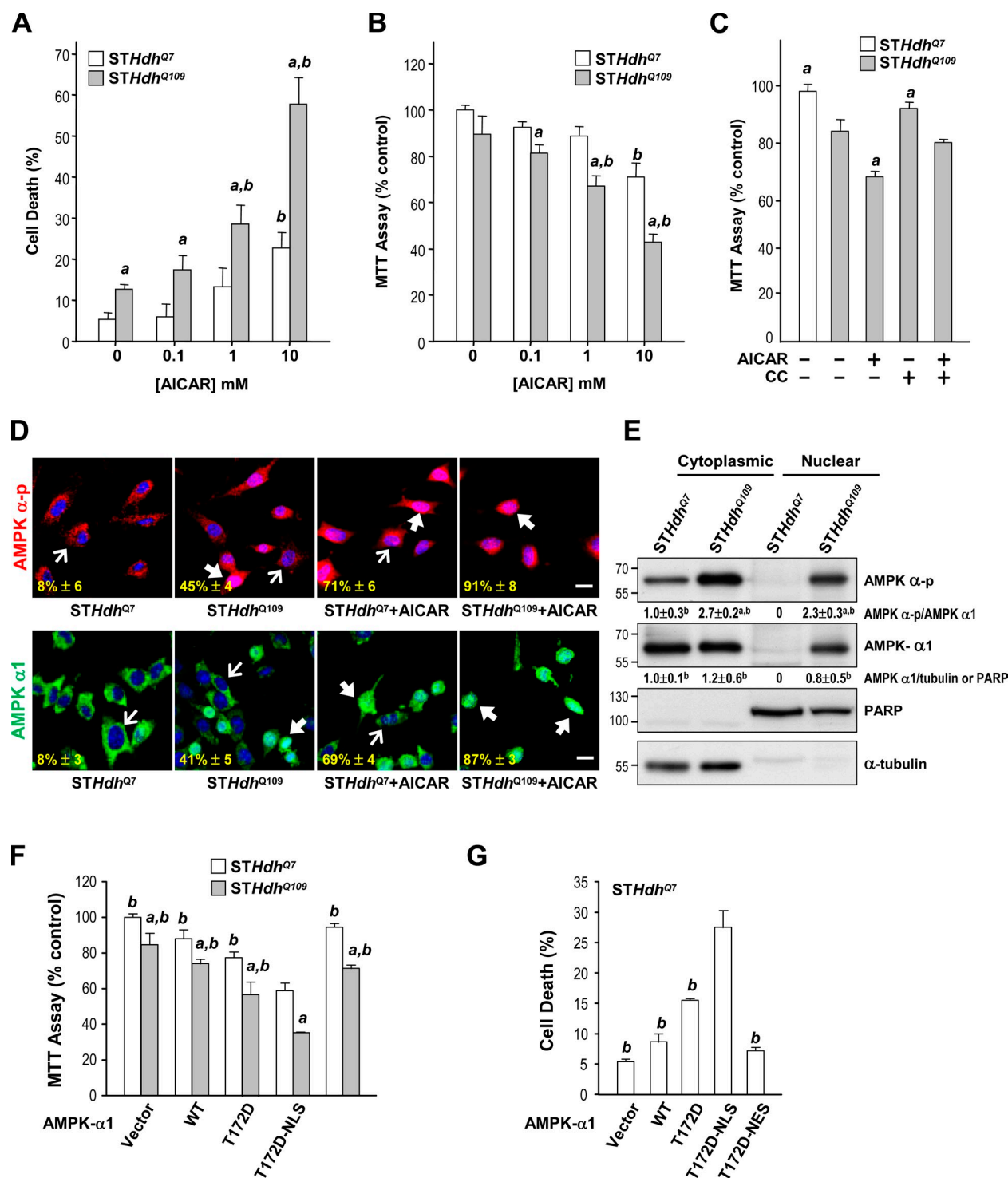
Figure 5. **Expression of mHtt leads to activation and nuclear enrichment of AMPK-α1, which plays a detrimental role in striatal cells.** (A–C, F, and G) Cells were treated with or without the indicated reagents (1 mM AICAR and 10 μM CC) for 24 h. Cell survival was determined by a flow cytometry–based analysis (A and G) or MTT reduction assay (B, C, and F). For the MTT assay, values of the indicated cells were normalized to those of untreated or vector-transfected ST*Hdh*^Q7^ cells. Data are presented as the mean ± SEM of three independent experiments. (A and B) a, P < 0.05 between ST*Hdh*^Q7^ and ST*Hdh*^Q109^; b, P < 0.05 versus untreated cells. (C) a, P < 0.05 versus AICAR-treated cells. (D) Immunofluorescence staining of AMPK-α-p and AMPK-α1 was conducted. Nuclei were stained with Hoechst (blue). The numbers in the bottom left corners are the percentages of cells expressing nuclear AMPK-α-p or AMPK-α1 and were identified by nuclear AMPK-α-p or AMPK-α1 normalized to total AMPK-α-p or AMPK-α1–positive cells. Thin arrows mark cells containing AMPK, which is located mostly in cytoplasmic regions. Thick arrows mark cells with nuclei enriched with AMPK. Bars, 20 μm. (E) Cytoplasmic and nuclear fractions of ST*Hdh*^Q7^ and ST*Hdh*^Q109^ cells were assessed by Western blot analyses. PARP and α-tubulin were respective markers for the nuclear and cytoplasmic fractions. Molecular mass is indicated in kilodaltons. a, P < 0.05 versus ST*Hdh*^Q7^ cytoplasmic fractions; b, P < 0.05 versus ST*Hdh*^Q7^ nuclear fractions. (F and G) Cells were transfected with the indicated construct for 48 h. a, P < 0.05 between ST*Hdh*^Q7^ and ST*Hdh*^Q109^ cells; b, P < 0.05 versus cells transfected with AMPK-α1-T172D-NLS. (D–G) Data are presented as the mean ± SEM of three independent experiments.

Nuclear AMPK-α1 induces cell death by down-regulating Bcl2 in striatal cells

Among the AMPK-regulated survival genes, *Bcl2* is implicated in the pathogenesis of HD (Zhang et al., 2003). Analyses using Western blot assays and a reverse transcription quantitative PCR (qPCR) technique showed that levels of the Bcl2 protein and *Bcl2* transcript in the striatum of R6/2 mice were markedly lower than those in WT mice (Fig. 8, A and B). Similarly, levels of *Bcl2* transcripts and the Bcl2 protein were also lower in the ST*Hdh*^{Q109} cells than in ST*Hdh*^{Q7} cells (Fig. 8, C and D). Inhibition of AMPK in ST*Hdh*^{Q109} cells with an AMPK inhibitor, CC, normalized the reduced level of Bcl2 protein, whereas activation of AMPK by AICAR reduced the level of the Bcl2 protein (Fig. 8 D). Next, we transfected AMPK-α1-T172D-NLS, AMPK-α1-T172D-NES, or AMPK-α1-T172A-NLS into ST*Hdh*^{Q7} cells and assessed their effects on Bcl2 expression. Only the nucleus-restricted positive AMPK-α1 mutant (AMPK-α1-T172D-NLS) caused significant reductions in levels of *Bcl2* transcript and Bcl2 proteins in ST*Hdh*^{Q7} cells (Fig. 8, E and F). Nuclear accumulation of AMPK-α1 promoted by mHtt thus causes down-regulation of Bcl2. This suppression of Bcl2 is functionally important because the overexpression of Bcl2 in ST*Hdh*^{Q109} cells enhanced their survival and prevented AICAR- and nuclear AMPK-α1–induced cell death (Fig. 8, G–I). Collectively, these data suggest that Bcl2 plays a critical role in nuclear AMPK-α1–mediated striatal cell death.

A beneficial reagent (CGS) protects striatal cells from mHtt-mediated toxicity via interfering with the detrimental action of AMPK-α1

AMPK was shown to cause cell death by reducing the phosphorylation of cAMP response element binding (CREB) at Ser^{133} and Ser^{129}, thereby inhibiting the CREB-mediated transcription of several survival genes (including *Bcl2*; Horike et al., 2008). Because PKA directly phosphorylates CREB at Ser^{133}, we hypothesized that activation of the cAMP–PKA pathway would increase the expression of Bcl2 and thus avert the damaging effects of AMPK. We previously showed that treatment of R6/2 mice with an A$_{2A}$R-selective agonist (CGS) prevented several major symptoms of HD (Chou et al., 2005). The major signal evoked by activation of the A$_{2A}$R is the cAMP–PKA pathway (Chern et al., 1993). Consistent with our hypothesis, we found that the reduction in *Bcl2* transcripts in the striatum of R6/2 mice was rescued by chronic CGS (2.5 mg/kg of body weight) treatment (Fig. 9 A). Treating ST*Hdh*^{Q109} cells with 10 μM CGS for 24 h also markedly increased levels of *Bcl2* transcripts (Fig. 9 B). This enhancing effect of CGS was mediated through the A$_{2A}$R in a PKA-dependent manner because an A$_{2A}$R-selective antagonist (8-[-3-chlorostyryl]-caffeine [CSC]; 20 μM) and a PKA inhibitor (H89; 10 μM) suppressed the ameliorating effect of CGS on *Bcl2* expression (Fig. 9 B). Consistent with the beneficial effects of CGS on R6/2 mice (Chou et al., 2005), CGS treatment also enhanced the survival of ST*Hdh*^{Q109} cells after AICAR treatment (Fig. 9, E and F). As shown in Fig. 9 C, the level of CREB phosphorylation at Ser^{133} was lower in ST*Hdh*^{Q109} cells than in ST*Hdh*^{Q7} cells. The AMPK inhibitor CC increased
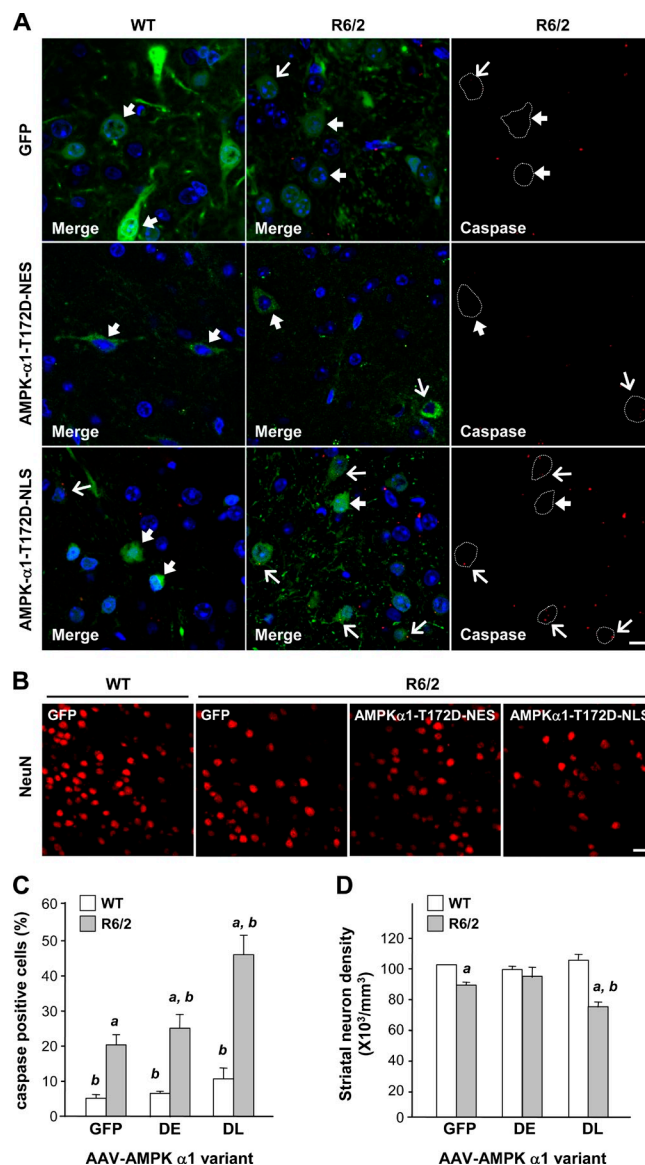

Figure 6. Nuclear localization of active AMPK-α1 causes striatal degeneration in R6/2 mice. (A and B) Mice were intrastriatally injected with an AAV carrying a GFP, AMPK-α1-T172D-NLS-YFP (DL), or AAV-AMPK-α1-T172D-NES-YFP (DE) at the age of 7 wk. 5 wk after the injection, brain sections were harvested and analyzed for neuronal degeneration. (A) Infected cells were identified by the expression of AAV-GFP (top, green) or AMPK-α1 mutant–YFP (middle and bottom, green) as indicated. For clarity, examples of infected striatal cells of R6/2 mice are marked by white dashed lines and are shown at the right. Levels of active caspases (A, red) and NeuN (B, red) in the striatum of the indicated mice (*n* = ∼3–6 for each condition) are shown. Nuclei were stained with Hoechst (A, blue). Thick arrows mark AAV-infected cells that were negative for active caspases. Thin arrows mark AAV-infected cells that were positive for active caspases. Bars, 20 μm. (C and D) The histograms show the integrated intensity of active caspases (C) and the number of striatal neurons (D). Data are presented as the mean ± SEM. At least 1,000 cells from each animal were analyzed. a, P < 0.05 between WT and R6/2 mice; b, P < 0.05 versus HD-AAV-GFP mice.

the phosphorylation of CREB in ST*Hdh*^{Q109} cells. These data show that CREB functions downstream of AMPK in striatal cells that express mHtt. As expected, stimulation of the A$_{2A}$R with CGS markedly increased the phosphorylation of CREB, which was blocked by the PKA inhibitor H89 (Fig. 9 C). Most importantly, an inactive CREB mutant (CREB-S133A),
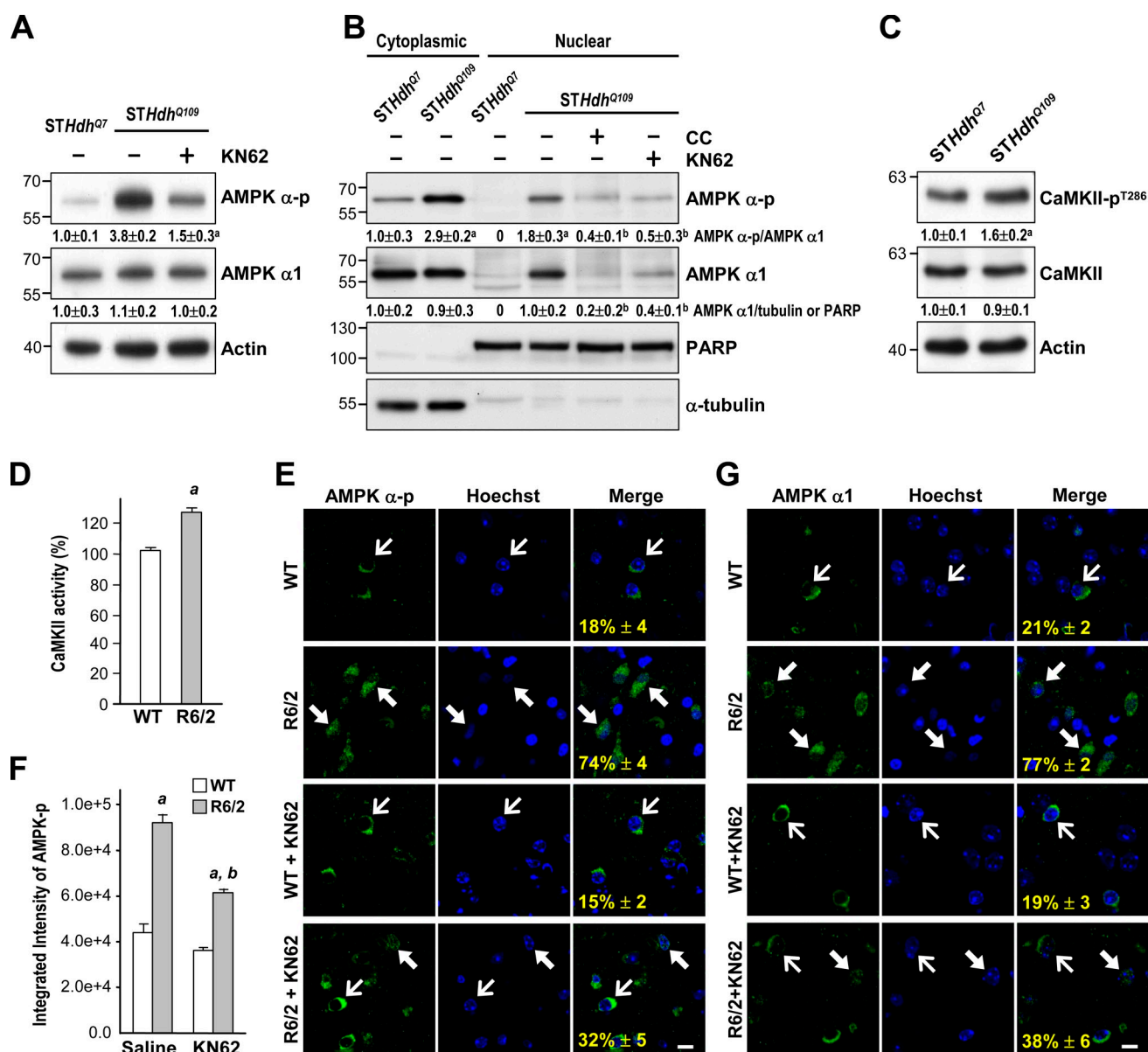
Figure 7. **Expression of mHtt causes the activation and nuclear enrichment of AMPK-α1 through a CaMKII-mediated pathway.** (A) Total lysates of ST*Hdh*[Q7] and ST*Hdh*[Q109] cells were assessed by Western blot analyses. Results were normalized to those of actin. a, P < 0.05 versus untreated ST*Hdh*[Q109] cells. (B) Cytosolic and nuclear fractions were harvested from ST*Hdh*[Q7] and ST*Hdh*[Q109] cells and assessed by Western blot analyses. PARP and α-tubulin were markers for the nuclear and cytoplasmic fractions, respectively. a, P < 0.05 versus untreated ST*Hdh*[Q7] cells; b, P < 0.05 versus untreated ST*Hdh*[Q109] cells. (C) Total lysates of ST*Hdh*[Q7] and ST*Hdh*[Q109] cells were assessed by Western blot analyses. Results were normalized to those of actin. a, P < 0.05 versus untreated ST*Hdh*[Q7] cells. Molecular mass is indicated in kilodaltons. (D) Total striatal lysates of 12-wk-old mice were assayed for CaMKII activity. Values are expressed as percentages of the CaMKII activity in WT mice. a, P < 0.05 between WT and R6/2 mice. (A–D) Data are presented as the mean ± SEM of three independent experiments. (E and G) 10-wk-old mice (n = ∼3–6 for each condition) were intrastriatally injected with KN62 (10 μg per mouse) or saline. 1 d after injection, brain sections were harvested to analyze the expressions of AMPK-α-p (E, green) and AMPK-α1 (G, green). Nuclei were stained with Hoechst (blue). The numbers shown in the bottom left corners of the merged images are the percentages of cells expressing nuclear AMPK-α-p (E) or AMPK-α1 (G) and were identified by nuclear AMPK-α-p (E) or AMPK-α1 (G) normalized to total AMPK-α-p or AMPK-α1–positive cells. Data are presented as the mean ± SEM. At least 200 cells from each animal were analyzed. Thin arrows mark cells in which AMPK-α-p is located mostly in the cytoplasmic region. Thick arrows mark cells with nuclear enrichment of AMPK-α-p. Bars, 20 μm. (F) The histogram shows the fluorescence intensity of AMPK-α-p (n = 6 for each condition). Data are presented as the mean ± SEM. a, P < 0.05 between WT and R6/2 mice; b, P < 0.05 versus R6/2-saline mice.

in which Ser[133] is converted to Ala (Parker et al., 1996), inhibited the increase in *Bcl2* induced by CGS (Fig. 9 B). These data show that the phosphorylation of CREB at Ser[133] by PKA plays a vital role in $A_{2A}R$-mediated regulation of Bcl2 in striatal cells.

Consistent with the ability of CGS to increase the phosphorylation of CREB (Fig. 9 C), CGS also effectively protected

ST*Hdh*[Q109] cells from cell death (Fig. 9, D–F). Down-regulation of AMPK-α1 using small hairpin RNA elevated the survival of ST*Hdh*[Q109] cells to a similar level as that of ST*Hdh*[Q7] cells and blunted the effect of CGS (Fig. 9 D). Similarly, an antagonist of the $A_{2A}R$ (CSC), a PKA inhibitor (H89), and a dominant-negative mutant of CREB (CREB-S133A) blocked the ameliorating effects of CGS (Fig. 9, E and F), which supports the notion that
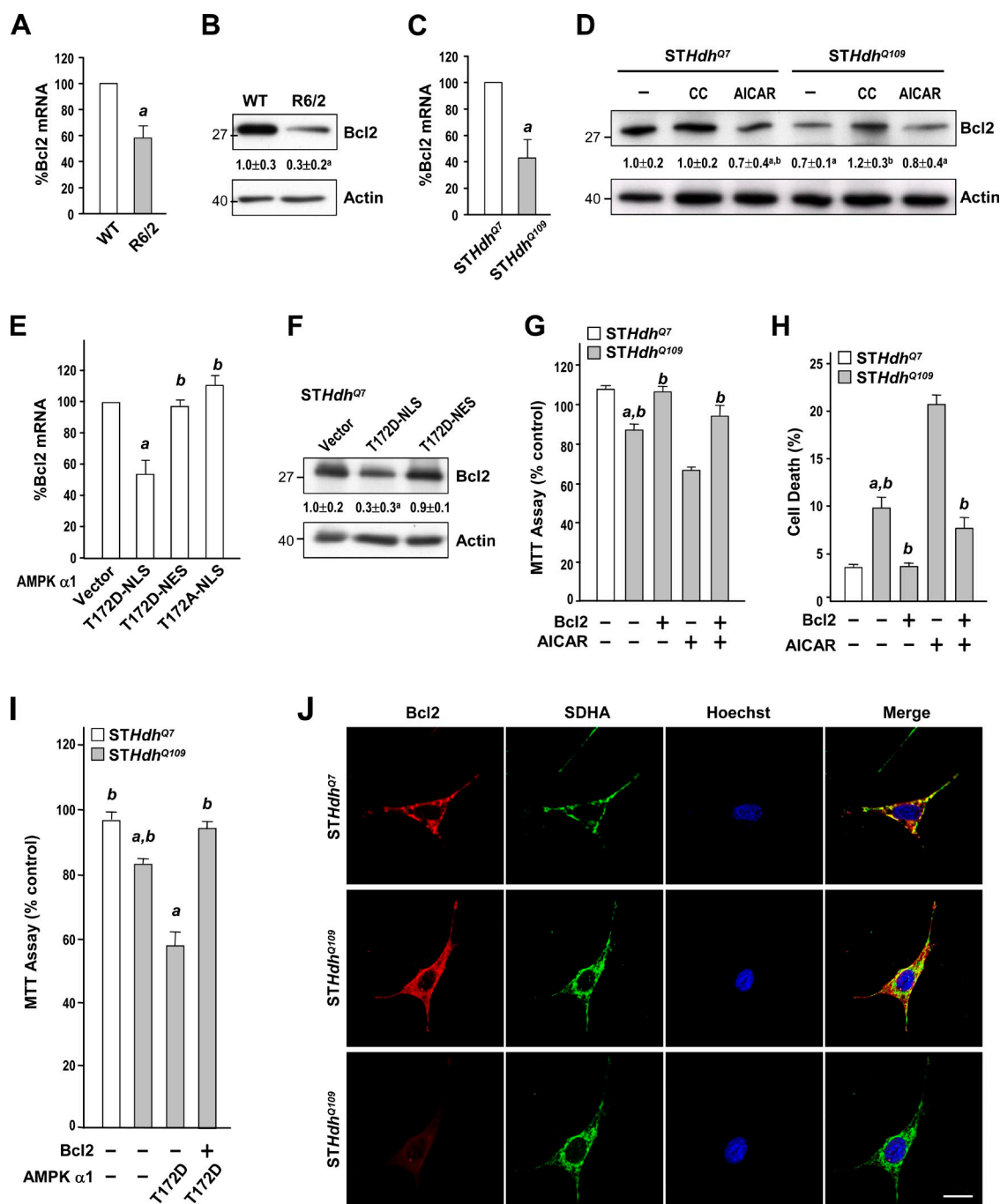
Figure 8. **Nuclear enrichment and activation of AMPK-α1 mediate the suppression of Bcl2 by mHtt.** (A, C, and E) Total RNA was harvested from the striatum of 12-wk-old mice (A) and striatal cell lines (C and E) to analyze transcript levels of *Bcl2* using reverse transcription qPCR. Transcript levels of Bcl2 were normalized to those of GAPDH. a, $P < 0.05$. (B, D, and F) Total protein lysates were prepared from the striatum of 12-wk-old mice (B) and striatal cell lines (D and F) for Western blot analyses to determine protein levels of Bcl2. Protein levels of Bcl2 were normalized to that of actin. Molecular mass is indicated in kilodaltons. (D) Cells treated with 1 mM AICAR and 10 µM CC as indicated for 24 h. a, $P < 0.05$ versus untreated ST*Hdh*^{Q7} cells; b, $P < 0.05$ versus untreated cells. (E and F) ST*Hdh*^{Q7} cells were transfected with the indicated construct and then incubated for 48 h. a, $P < 0.05$ versus cells transfected with the empty vector (pcDNA3.1); b, $P < 0.05$ versus cells transfected with AMPK-α1-T172D-NLS. (G and H) Cells were transfected with an empty vector (pcDNA3.1) or an expression construct of Bcl2 for 24 h followed by a 24-h incubation with 1 mM AICAR. Cell survival was determined by an MTT assay (G) and a flow cytometry–based analysis (H). a, $P < 0.05$ between ST*Hdh*^{Q7} and ST*Hdh*^{Q109} cells; b, $P < 0.05$ versus AICAR-treated vector-expressing cells. (I) ST*Hdh*^{Q109} cells were transfected with the indicated constructs for 48 h. Cell survival was determined by an MTT assay. a, $P < 0.05$ between ST*Hdh*^{Q7} and ST*Hdh*^{Q109} cells; b, $P < 0.05$ versus cells transfected with AMPK-α1-T172D. (A–I) Data are presented as the mean ± SEM of three independent experiments. (J) Immunofluorescence staining of Bcl2 (top and middle, short exposure; bottom, long exposure) and a mitochondrial marker (succinate dehydrogenase [SDHA]) in ST*Hdh*^{Q7} and ST*Hdh*^{Q109} cells was conducted as indicated. Nuclei were stained with Hoechst (blue). Bar, 20 µm.
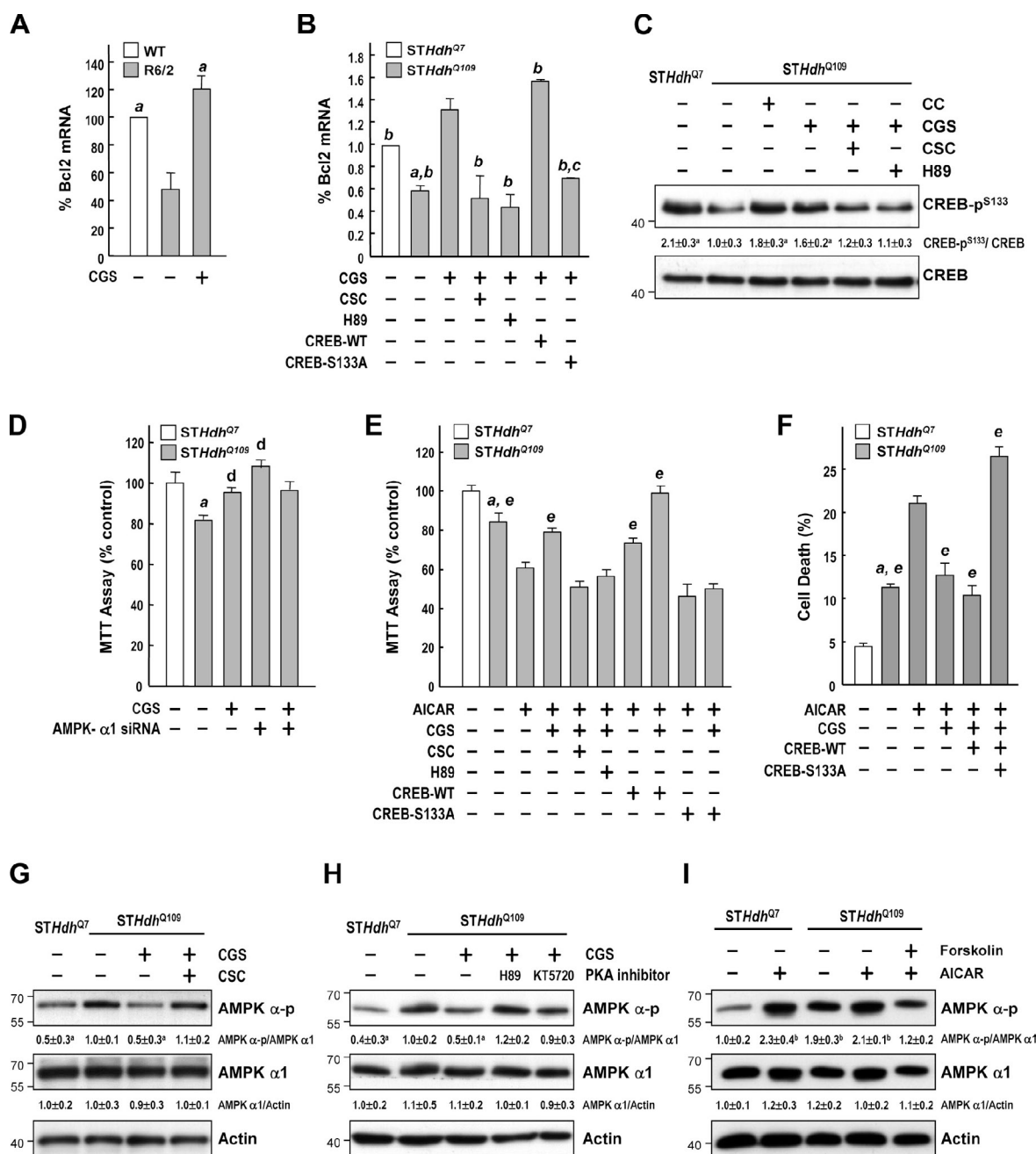
Figure 9. **Stimulation of the A$_{2A}$R rescued AMPK-mediated suppression of Bcl2 via a PKA–CREB-dependent pathway.** (A) Mice were treated daily with CGS (2.5 mg/kg of body weight, i.p.) or vehicle for 6 wk from the age of 4 wk. Transcript levels of *Bcl2* assessed by reverse transcription qPCR were normalized to those of GAPDH. a, P < 0.05 versus R6/2 mice. (B and D–F) Cells were transfected with the indicated constructs for ~24–48 h and then treated with the indicated reagents for 24 h. Transcript levels of *Bcl2* assessed by reverse transcription qPCR were normalized to those of GAPDH (B). a, P < 0.05 versus untreated ST*Hdh*^{Q7} cells; b, P < 0.05 versus ST*Hdh*^{Q109} cells treated with CGS; c, P < 0.05 with a specific comparison between cells transfected with CREB-WT and CREB-T133A; d, P < 0.05 versus untreated ST*Hdh*^{Q109} cells; e, P < 0.05 versus AICAR-treated cells. (D–F) Cell survival was determined using an MTT assay (D and E) and flow cytometry–based analysis (F). (C and G–I) Cells were treated with the indicated reagents for 24 h. Levels of phosphorylated CREB (CREB-p^{S133}) were assessed by Western blot analyses and normalized to those of total CREB (C). Levels of AMPK-α-p^{T172} and AMPK-α1 were assessed by Western blot analyses and normalized to those of actin (G–I). Molecular mass is indicated in kilodaltons. a, P < 0.05 versus untreated ST*Hdh*^{Q109} cells; b, P < 0.05 versus untreated ST*Hdh*^{Q7} cells. (A–I) Data are presented as the mean ± SEM of three independent experiments.

activation of the A$_{2A}$R rescues the AMPK-mediated detrimental effects via the PKA–CREB pathway.

Next, we showed that CGS treatment suppressed AMPK phosphorylation/activation (Fig. 9 G). The suppressive effect of CGS on AMPK activation was reduced by an A$_{2A}$ antagonist (CSC) and two PKA inhibitors (H89 and KT5720), indicating

that the effects of CGS are mediated through the A$_{2A}$R and PKA (Fig. 9 H). The direct activation of adenylyl cyclases with forskolin also inhibited AMPK phosphorylation during AICAR treatment (Fig. 9 I). PKA thus mediates the rescue effect of the A$_{2A}$R on the detrimental role of AMPK-α1 in striatal neurons. CGS treatment at an earlier time point (6 h) also effectively
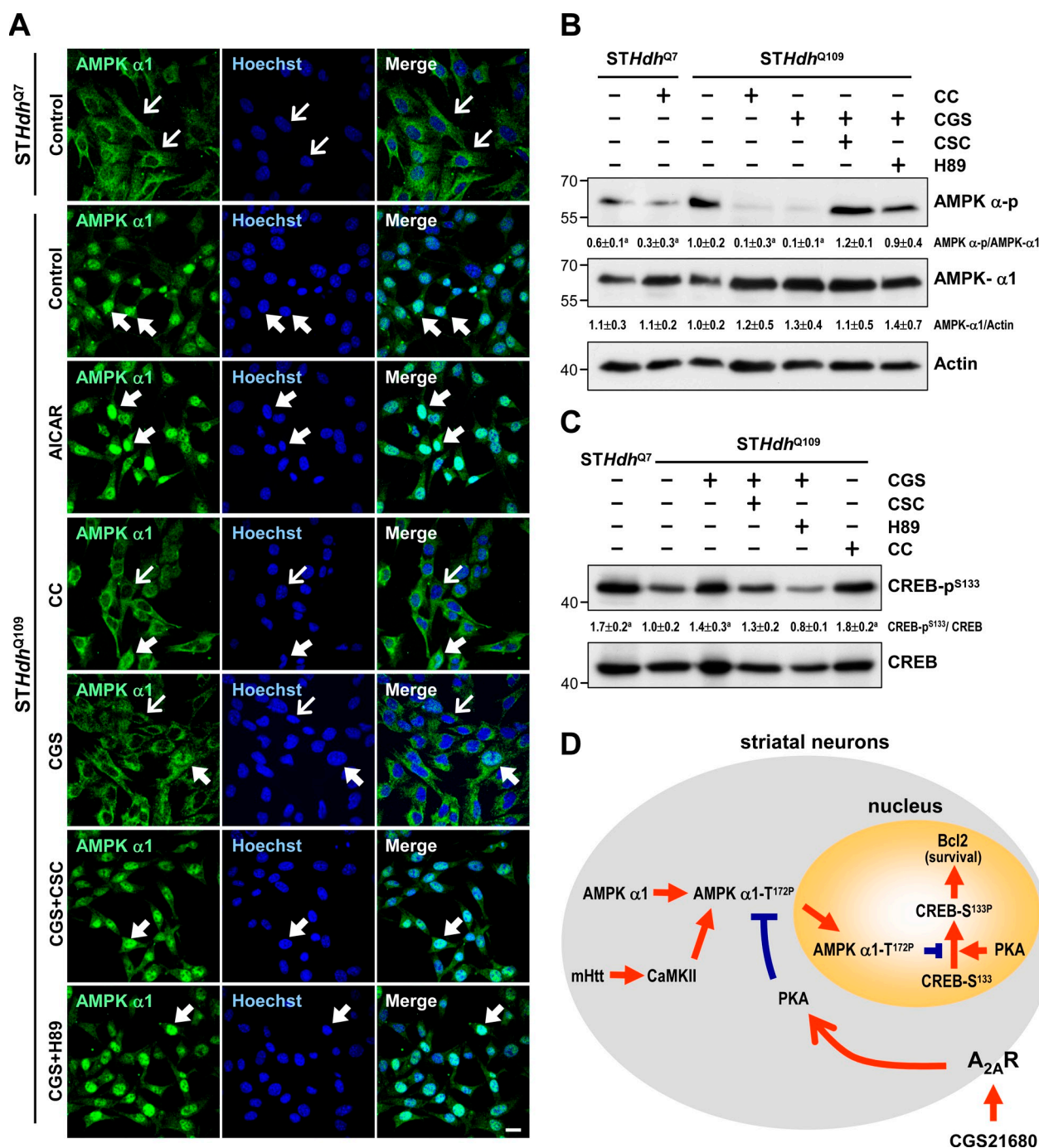
Figure 10. **Activation of the A$_{2A}$R using CGS inhibits the translocation of AMPK-α1 into nuclei of STHdh^{Q109} cells.** (A–D) Cells were treated with or without the indicated reagents (10 μM CC, 10 μM CGS, 10 μM H89, 20 μM CSC, and/or 1 mM AICAR) for 6 h. (A) Immunofluorescence staining of AMPK-α1 was conducted. Nuclei were stained with Hoechst. Thin arrows mark cells in which AMPK-α1 is located mostly in the cytoplasmic region. Thick arrows mark cells with nuclear enrichment of AMPK-α1. Bar, 20 μm. (B) Total lysates were analyzed for Western blot analyses. Results were normalized to actin. (C) Levels of phosphorylated CREB (CREB-p^{S133}) were assessed by Western blot analyses and normalized to those of total CREB. (B and C) Data are presented as the mean ± SEM of three independent experiments. Molecular mass is indicated in kilodaltons. a, $P < 0.05$ versus untreated STHdh^{Q109} cells. (D) A schematic representation of signaling pathways that mediate the action of A$_{2A}$R in rescuing the detrimental effect of AMPK-α1 via a PKA–CREB-dependent pathway in the presence of mHtt. The gray circle and orange circle represent the soma and nucleus of striatal neurons, respectively.

suppressed activation of AMPK, retained AMPK-α1 in the cytoplasm, and reversed the lower phosphorylation level of CREB in STHdh^{Q109} (Fig. 10, A–C). Together with observations that CGS treatment protected striatal cells (Fig. 9, D–F), this finding supports our hypothesis that prevention of the nuclear accumulation of AMPK-α1 is beneficial to striatal cells.

Discussion

In this study, we demonstrated that mHtt activates AMPK-α1 and translocates it into the nuclei of two striatal cell lines that express mHtt and into nuclei of striatal neurons in mice and humans with HD (Figs. 1 and S1 and Table I). The observation that

increased nuclear accumulation of AMPK-α1 was found in two affected brain areas of HD patients (Figs. 1 [A and B] and S1 [A–C]) demonstrates the clinical relevance of this finding. Expression of polyQ-expanded mHtt appeared to enhance the activity of CaMKII and subsequently activated and promoted the nuclear enrichment of AMPK-α1 (Fig. 7). Such nuclear enrichment of activated AMPK-α1 caused a reduction in the expression of *Bcl2* in a CREB-dependent manner and promoted cell death. A beneficial reagent, CGS, activated the cAMP–PKA pathway and protected striatal neurons by attenuating the detrimental role of AMPK-α1 via at least two independent routes. First, PKA phosphorylated CREB at Ser[133] and consequently increased the expression of Bcl2. Second, PKA suppressed the activity of AMPK, which in turn prevented the nuclear translocation of AMPK-α1 and the subsequent down-regulation of Bcl2 expression (Fig. 10 D). Our findings provide insights into a novel mechanism by which energy deficiency significantly contributes to HD pathogenesis and shed new light on the protective effects of cAMP-elevating reagents in a mouse model of HD (Chou et al., 2005; Giampà et al., 2009).

The role of AMPK activation in HD pathogenesis appears highly complex. An earlier study showed that a 5-wk treatment with metformin extends the shortened life span and reduces the hind limb clasping of male R6/2 mice (Ma et al., 2007). Except for the validation of AMPK activation in the striatum using Western blot analyses, no histological examination of brains of metformin-treated HD mice was conducted. These authors concluded that the site of metformin's action remains unclear and that the improvement in the functions of peripheral systems might contribute to this metformin-mediated beneficial effect (Ma et al., 2007). To assess the pathological role of AMPK-α1 in striatal neurons during HD progression, we used multiple approaches to evaluate the brains of HD mice treated with AICAR or AMPK mutants in the present study. It is important to note that besides activating AMPK, AICAR also has other effects. For example, AICAR induces astroglial differentiation of neural stem cells via activating an AMPK-independent and JNK–STAT3-mediated pathway (Zang et al., 2008). Nonetheless, the harmful role of AMPK-α1 in striatal cells expressing mHtt was clearly validated using both pharmacological (AICAR and CC) and genetic tools (dominant-positive or -negative mutants and siRNA of AMPK-α1). Data from 3D MRI, brain weights, histological examinations, behavioral changes, and expression profiles of apoptosis/survival signals consistently showed that activation of AMPK-α1 in striatal neurons potentiates striatal atrophy, neuronal loss, and motor dysfunction evoked by mHtt (Figs. 3, 4, and 6). Given that mHtt selectively activates AMPK-α1 in the striatum of HD animals (Fig. 1, E and F) and that the heterotrimeric subunit compositions of AMPK in the brain and peripheral tissues (e.g., the muscles) might greatly differ (Stapleton et al., 1996; Wojtaszewski et al., 2005), modulation of AMPK-mediated pathways by mHtt might differ in different tissues. Further studies are required to delineate the tissue-specific regulation of AMPK and its pathogenic consequences during the progression of HD.

In addition to its role in peripheral metabolic diseases (e.g., diabetes and cardiac ischemia), AMPK has also attracted much attention lately in the context of neurodegenerative diseases. Specifically, AMPK-α is highly enriched in primary cortical and hippocampal neurons under ischemic stress (McCullough et al., 2005) and in a transgenic model of AD (Lopez-Lopez et al., 2007). Numerous studies showed that AMPK plays a proapoptotic role in various cell types, such as cortical neurons, hepatocytes, neuroblastoma cells, and mouse insulinoma 6 cells (Meisse et al., 2002; Garcia-Gil et al., 2003; Kefas et al., 2003; Jung et al., 2004). Besides modulating Bcl2 expression, activation of AMPK by isotope-coded affinity tag may also alter the activity of other prosurvival genes/proteins in HD. Using Western blot analyses, we found that the activities of two prosurvival proteins (ERK1/2 and Akt) were lower in the striatum of 12-wk-old R6/2 mice than those of WT mice (unpublished data). A daily i.p. injection of AICAR (400 mg/kg of body weight) for 5 wk further reduced the phosphorylation/activation of ERK1/2 in the striatum of R6/2 mice by 20 ± 5% (mean ± SEM, P < 0.05, three independent experiments, Student's *t* test). Mild suppression of ERK1/2 therefore might also contribute to AMPK-α1–evoked toxicity in striatal cells. In contrast, the same AICAR treatment did not affect the phosphorylation/activation of Akt (unpublished data). It remains to be determined whether the AICAR-mediated effect on the phosphorylation/activation of ERK1/2 is direct or indirect. Given the therapeutic potential of prosurvival genes/proteins in HD, future studies are warranted to investigate the complex regulation of these prosurvival signals by AMPK during HD progression.

Given the key regulatory role of AMPK in energy homeostasis, AMPK is believed to fine tune survival and cell death upon being stressed via modulating multiple cellular machineries. In contrast to the detrimental role of AMPK-α1 in HD as shown in the present study, protective roles of AMPK were also reported in several different cell types (Shaw et al., 2007). For example, AMPK activation mediates autophagy-enhanced survival during oxidative stress or treatment with anticancer drugs. Several downstream targets of AMPK are also known to play protective roles against stress under defined conditions and in specific tissues. Among them, PGC-1α is of particular interest. PGC-1α is a transcription factor important in many metabolic pathways and is known to play a protective role in HD (Cui et al., 2006). In muscles of WT mice, activation of AMPK directly phosphorylates and activates PGC-1α and enhances mitochondrial biogenesis (Jäger et al., 2007; Chaturvedi et al., 2009). However, the activity of AMPK is not elevated by mHtt in muscles of NLS-N171-82Q mice (a transgenic mouse model of HD), nor does energy depletion activate AMPK or PGC-1α in muscles of HD mice, demonstrating an impaired AMPK pathway in the muscles of HD animals (Chaturvedi et al., 2009). The role of AMPK activation in regulating PGC-1α in the brains of mice or humans with HD is currently unknown and warrants further investigation.

Our finding that mHtt selectively activates AMPK-α1 but not AMPK-α2 is intriguing. Such selective regulation of the AMPK isoform in other pathophysiological conditions was previously reported. Specifically, acute exercise in patients with type 2 diabetes or depletion of phosphocreatine in young nondiabetic subjects led to activation of AMPK-α2 but

not AMPK-α1 in the muscles (Fujii et al., 2000; Musi et al., 2001). It was hypothesized that AMPK-α1 and AMPK-α2 might have different substrate specificities and play distinct physiological roles in human skeletal muscles (Weekes et al., 1993; Fujii et al., 2000). However, no significant difference between the catalytic activities of AMPK-α1 and AMPK-α2 was found when assessed using an artificial substrate (Woods et al., 1996). Further investigation is needed to determine whether the β and γ subunits of AMPK determine the substrate specificity by targeting specific binding proteins under various pathophysiological conditions.

To assess whether the activation and nuclear accumulation of AMPK-α1 in the brain is a common pathogenesis of polyQ diseases, we transfected ST14A cells with the expression construct of spinocerebellar ataxia type 3 (SCA3; Chai et al., 1999), which harbors a normal (28) or an expanded (84) number of CAG repeats and was fused to hrGFP. As expected, expression of SCA3-84Q:hrGFP, but not SCA3-28Q:hrGFP, formed aggregates (Fig. S4 A). However, the expression of neither SCA3-84Q:hrGFP nor SCA3-28Q:hrGFP triggered activation and/or nuclear enrichment of AMPK (Fig. S4 B), suggesting that regulation of AMPK-α1 in the brain of HD is mHtt specific. The molecular mechanism underlying the nucleocytoplasmic shuttling of AMPK-α1 in striatal neurons that express mHtt is currently unknown. The ERK1/2 pathway might warrant investigation because a previous study suggested that it controls the cellular localization of AMPK in HeLa cells under stressful conditions (Kodiha et al., 2007). Although we cannot completely exclude the possibility, it is unlikely that mHtt directly binds with AMPK-α1 and thus leads to nuclear enrichment of AMPK-α1 because we failed to coimmunoprecipitate AMPK-α1 with mHtt in an attempt to detect a direct interaction between AMPK-α1 and mHtt (Fig. S5, A and B). Moreover, neither AMPK-α1 nor AMPK-α2 was detected in aggregates of mHtt in the striatum of R6/2 mice as assessed by a filter retardation assay (Fig. S5 C), suggesting that AMPK might not interact with mHtt and form aggregates. Another component that was implicated in cellular localization and nuclear redistribution of AMPK is its β1 subunit (Warden et al., 2001; Hedbacker and Carlson, 2006). We thus examined the subcellular localization and phosphorylation level of AMPK-β1 in striatal cells expressing mHtt and found no difference between STHdh^{Q7} and STHdh^{Q109} cells (Fig. S5, D and E). The exact molecule that mediates the activity-dependent nuclear enrichment of AMPK-α1 remains to be identified in the future.

It will be of interest to examine whether the nuclear translocation of AMPK-α1 contributes to the pathogenic mechanisms of other brain diseases and traumas in which AMPK overactivation was reported (McCullough et al., 2005; Lopez-Lopez et al., 2007). Y. Chen et al. (2009) earlier demonstrated that metformin enhances the biogenesis of amyloid peptides, which is mediated by transcriptional up-regulation of β-secretase (BACE1) in an AMPK-dependent pathway and which might worsen the progression of AD. Because the transcriptional regulation of BACE1 by AMPK might occur in the nucleus, it will be important to identify the subcellular localization and the identity of the AMPK-α isoform that is involved in

AD pathogenesis. Caution might be exercised when prescribing general AMPK activators for diabetic patients who also exhibit symptoms of neurodegenerative diseases with elevated AMPK activity in the brain (Chou et al., 2005; McCullough et al., 2005; Lopez-Lopez et al., 2007). Given the potential isoform-specific functions and regulation of the AMPK isoform as shown in the present study and in other studies (Fujii et al., 2000; Musi et al., 2001), development of isoform-specific AMPK activators and inhibitors will be of value for future clinical applications.

Materials and methods

Cell cultures
Striatal progenitor ST14A, STHdh^{Q7}, and STHdh^{Q109} cell lines were gifts from E. Cattaneo and M. Valenza (University of Milano, Milano, Italy). These cells were maintained in an incubation chamber gassed with 5% CO_2-95% air at 33°C (Cattaneo and Conti, 1998). Cells were transfected using Lipofectamine 2000 (Invitrogen) following the manufacturer's protocol and were cultured for another 48 h in the presence or absence of the indicated reagents.

Constructs
The pcDNA3.1-Htt-(Q)$_{25}$-hrGFP and pcDNA3.1-Htt-(Q)$_{109}$-hrGFP constructs encoding an N-terminal fragment of Htt with the indicated number of polyQ residues fused to a gene encoding hrGFP were created as previously described (Chiang et al., 2005). Mouse AMPK-α1 cDNA was amplified from mouse brain cDNA and subcloned into the BamHI site of pcDNA3.1 (Invitrogen). The dominant-positive mutant of AMPK-α1 (AMPK-α1-T172D) and the dominant-negative mutant of AMPK-α1 (AMPK-α1-T172A) were created by mutating the Thr^{172} residue into Asx and Ala, respectively (Stein et al., 2000). AMPK-α1-T172D-NLS/NES and AMPK-α1-T172A-NLS/NES were created by fusing the corresponding AMPK-α1 variant to an NLS (PKKKRKV) or an NES (LPPLERLTLDS; Cong and Varmus, 2004). The NES and NLS constructs were gifts from W.-Y. Tarn (Institute of Biomedical Sciences, Academia Sinica, Taipei, Taiwan). The CREB constructs were a gift from H.-M. Shih (Institute of Biomedical Sciences, Academia Sinica, Taipei, Taiwan).

Construction, production, and intrastriatal injection of adeno-associated viral vectors
Pseudotyped AAV8 vectors were generated by transient transfection of HEK293 cells with the target plasmid along with helper plasmids as detailed in Xiao et al. (1998). The DNA fragment that encodes NLS-EYFP-AMPK-α1 or NES-EYFP-AMPK-α1 was created by fusing an NLS (PKKKRKV) or an NES (LPPLERLTLDS) to EYFP-AMPK-α1 by a PCR-based molecular biology technique, and this was subcloned into the NotI site of the AAV8 virus construct (pXX-UF1-CB; Pan et al., 2008). The physical vector titers of AAVs were assessed by determining the number of packaged vector genomes using a qPCR method as described in C.C. Chen et al. (2009). Titers of AAV-GFP, NLS-EYFP-AMPK-α1, and NES-EYFP-AMPK-α1 were 10^{11}/µl, 1.6 × 10^{11}/µl, and 1.8 × 10^{11}/µl, respectively.

For the in vivo expression of AMPK-α1, male mice were anesthetized with ketamine/xylazine (100 and 16 mg/kg i.p., respectively; Merial Laboratoire de Toulouse) and intrastriatally injected with the indicated AAV vector (1–2 µl) through a 10-µl syringe (Hamilton) fitted with a 26-gauge beveled hypodermic needle for 10 min at a rate of 200 nl/min. The anterior–posterior and medial–lateral coordinates were 0.5 and ±2 mm relative to the bregma, respectively. The dorsoventral coordinates were −3, −2.7, and −2.4 mm relative to the bregma.

Animals and AICAR administration
R6/2 mice (Mangiarini et al., 1996) were originally obtained from The Jackson Laboratory and were mated to female control mice (B6CBAFI/J). Offspring were identified by the PCR genotyping and sequencing technique of genomic DNA using primers located in the transgene (5′-CCGCTCAG-GTTCTGCTTTTA-3′ and 5′-GGCTGAGGAAGCTGAGGAG-3′). The number of CAG repeats of R6/2 mice used in this study was 212 ± 9. In total, 428 R6/2 transgenic mice and 321 WT littermate controls were used in the present study. Animals were housed at the Institute of Biomedical Sciences Animal Care Facility under a 12-h light/dark cycle. Animal experiments were performed under protocols approved by the Academia Sinica Institutional Animal Care and Utilization Committee. For in vivo AMPK activation

by AICAR, male mice were subcutaneously implanted with ALZET osmotic minipumps, which delivered AICAR (3 µg/animal/day) or saline into the striatum for 7 d. The anterior–posterior and medial–lateral coordinates were 0.5 and ±2 mm relative to the bregma, respectively. The dorsoventral co-ordinates were −3, −2.7, and −2.4 mm relative to the bregma.

Rotarod performance
Motor coordination was assessed using a rotarod apparatus assay (model 7600; Ugo Basile) at a constant speed of 12 rpm over a period of 2 min. All mice were tested three times per week. For each test, animals were placed in the apparatus before the initiation of rotation. Each mouse was given three trials for a maximum of 2 min for each trial.

Micro-MRI analysis
Whole-brain and 3D ventricle images of the animals were evaluated using a PharmaScan scanner (7 T; Bruker) as previously described (Chou et al., 2005), with modifications. Specifically, sagittal T2-weighted rapid-acquisition relaxation-enhanced images (with a repetition time of 2,000 ms, an effective echo time of 88.3 ms, a field of view of 3 cm, and a matrix of 256×128) were acquired and used to determine the location and length of the brain. T2-weighted 3D rapid-acquisition relaxation-enhanced scans were acquired axially (with a repetition time of 4,000 ms, an effective echo time of 80 ms, a voxel size of 5.71×10^{-6} cm, and a matrix of $256 \times 128 \times 32$). The VBR was measured by in vivo 3D MRI and calculated by dividing the value of the ventricle by that of the entire brain.

Immunohistochemistry and quantitation
Mice were anesthetized with an i.p. injection of 80 mg/kg sodium pento-barbital before intracardial perfusion with 4% PFA in 0.1 M phosphate buffer (PB; pH 7.4). After perfusion, the brains were carefully removed, fixed for 24 h in the same solution, immersed in 30% sucrose in 0.1 M PB for 2 d, and frozen on dry ice. Coronal serial sections were cut at 20 µm (HM430; Thermo Fisher Scientific) and stored in 6-well plates. Brain sections were immunohistochemically stained as previously described (Liu et al., 1998). In brief, brain sections were incubated overnight with the appropriate primary antibody in PBS containing 5% normal goat serum at 4°C and then incubated with the corresponding secondary antibody for 2 h at RT. The following primary antibodies were applied at the indicated dilutions in blocking buffer: anti-phospho–AMPK-α (1:100), anti–AMPK-α1 (1:200), anti–neuronal nuclei (NeuN; 1:1,000; Millipore), and anti-V5 (1:250). Nuclei were stained with Hoechst 33258. Slides were mounted using Vectashield (Vector Laboratories). Patterns of immunostaining were analyzed with a laser confocal microscope (LSM510; Carl Zeiss). Those containing the striatum (interaural 4.66 mm/bregma 0.86 mm to inter-aural 4.18 mm/bregma 0.38 mm) were stained for Nissl substance using cresyl violet or NeuN as previously described (Lee et al., 2009). In Nissl-stained brain sections, neurons appeared round and light purple. Unless otherwise stated, three pictures (marked by pink boxes) were taken of each striatal section as illustrated (Fig. 3 D, left) using a camera (Coolpix 5000; Nikon). Nine frames from three sections spaced evenly throughout the stria-tum (interaural 5.34 mm/bregma 1.54 mm to interaural 3.7 mm/bregma −0.1 mm) were analyzed for each animal by an investigator blind to the experimental condition. At least 500 and 700 cells from each animal were counted and measured to determine the size and number of neurons in the striatum, respectively. Neurons and signals of active caspases within count-ing frames of 266 × 200 µm were analyzed using 40× 1.0 or 2.0 NA or 63× 1.0 NA oil objective lenses (Nikon). Images were imported into ImageJ software (National Institutes of Health). To estimate the neuronal area, we outlined each neuronal soma at the plane of its nucleolus and measured the cross-sectional area using the ImageJ software as previously described (Chou et al., 2008). Quantitation of active caspases was conducted by laser confocal microscopy (LSM780; Carl Zeiss) and analyzed with the MetaMorph imaging system (Universal Imaging). The fluorochromes used in the present study were DAPI and Alexa Fluor 488, 568, and 633.

In vivo cell death assay
The SR-FLIVO in vivo apoptosis assay kit (ImmunoChemistry Technologies, LLC) was used to label apoptotic cells in vivo (Riol-Blanco et al., 2009). SR-FLIVO prepared as described in the manufacturer's manual was intrave-nously injected into the lateral tail vein of each mouse and was allowed to circulate in the body for 60 min before perfusion with 4% PFA in 0.1 M PB, pH 7.4, as described in the previous section. 20-µm coronal serial sections were used to analyze the activation of caspases by detecting the signal of SR-FLIVO using a laser confocal microscope (LSM780) with an excitation at 565 nm and an emission at 600 nm.

CaMKII activity assay
Total striatal lysate of three animals from each group of 12-wk-old R6/2 or WT mice was harvested for the CaMKII assay using the SignaTECT CaM kinase II Assay System (Promega). Tissues were homogenized in cold lysis buffer (20 mM Tris-HCl, pH 8.0, 2 mM EDTA and EGTA, 100 nM okadaic acid, 2 mM DTT, 1 mM PMSF, a protease inhibitor cocktail, and a phos-phorylation inhibitor cocktail). The homogenates were centrifuged at 12,000 g for 20 min at 4°C. Samples were incubated at 30°C for 3 min, and the reaction was terminated by adding termination buffer (7.5 M gua-nidine hydrochloride). The 10-µl reaction mixtures were then spotted onto a prenumbered square of the SAM Membrane (Promega), which was washed and dried according to the manufacturer's protocol. The amount of γ-[^{32}P]ATP incorporated into the CaMKII substrate was visualized by a PhosphorImager (Bio-Rad Laboratories). Data are presented as the percent-age of activity with respect to WT mice.

Cell death assays
Cell death was quantified by an MTT reduction assay and a flow cytometric analysis. The MTT reduction assay was conducted as described in Ju et al. (2005). In brief, MTT was dissolved in 50 mg/ml DMSO as a 100-fold stock solution. At the end of the experiments, cells were incubated in culture medium with 0.5 mg/ml MTT at 33°C for 2 h. The culture medium was then replaced with DMSO (100 µl in 96-well plates) to dissolve the MTT forma-zan precipitates, and the absorbance was measured at a wavelength of 570 nm in a microplate reader (OPTImax tunable plate reader; Molecular Devices). The flow cytometric analysis of apoptosis was conducted by stain-ing the cells with propidium iodide and sorting them with a flow cytometer as previously described (Nicoletti et al., 1991). In brief, after drug treat-ment, cells were rinsed with ice-cold PBS, fixed with 70% ethanol at −20°C for 1 h, and centrifuged at 500 g for 5 min at 4°C. After removal of the su-pernatant, the cell pellet was resuspended in 1 ml PBS containing 50 µg/ml propidium iodide plus 20 µg/ml RNase A, incubated in a 37°C water bath with gentle shaking in the dark, and filtered through a 70-µm nylon mesh to remove clumps. Apoptosis was analyzed using a flow cytometer (BD). The sub-G$_1$ fraction was quantified and designated the apoptotic portion. Data were analyzed with CellQuest software (BD). At least 10^4 gated cells were counted for each sample. The percentage of cells in the sub-G$_1$ phase of the cell cycle was estimated according to the DNA content.

SDS-PAGE and Western blotting
A Western blot analysis was performed as previously described (Chiang et al., 2007). In brief, proteins were electrophoretically fractionated through an 8 or 10% SDS polyacrylamide gel and electrotransferred onto polyvinylidene difluoride membranes (Millipore). The following pri-mary antibodies were applied to the blots at the indicated dilutions: anti–AMPK-α-p^{T172} (1:1,000; Cell Signaling Technology), anti–AMPK-α1 (1:1,000; Abcam), anti–AMPK-α2 (1:1,000; Abcam), anti–ERK1/2-p and anti-ERK1/2 (1:1,000; Cell Signaling Technology), anti–Akt-p and anti-Akt (1:1,000; Santa Cruz Biotechnology, Inc.), antitubulin (1:2,000; Sigma-Aldrich), anti–poly (ADP-ribose) polymerase (PARP; 1:2,000; Mil-lipore), anti-EM48 (Millipore), anti-V5 (1: 2,000; Millipore), antiactin (1:5,000; Santa Cruz Biotechnology, Inc.), anti-Bcl2 (1:1,000; Cell Sig-naling Technology), anti–procaspase 3, and anti–active caspase 3 (1:1,000; Cell Signaling Technology). The immunoreactive signals were detected with ECL reagents (PerkinElmer).

Filter retardation assay
SDS-insoluble mHtt aggregates were quantified as previously described (Chiang et al., 2007). In brief, brain tissues were suspended and homoge-nized in ice-cold radioimmunoprecipitation assay (RIPA) buffer (50 mM Tris-HCl, 0.25% sodium deoxycholate, 1% Triton X-100, 150 mM NaCl, 1 mM PMSF, 1 mM Na$_3$VO$_4$, 0.5 mg/ml aprotinin, 0.1 mM leupeptin, and 4 mM pepstatin), mixed with 2% SDS, and applied to OE66 membrane filters (0.2-mm pore size; GE Healthcare) through a slot-blot manifold (Bio-Rad Laboratories). The blots were blocked with 5% skim milk in PBS and in-cubated overnight with an anti-Htt antibody (1:500; Millipore) at 4°C followed by incubation with the corresponding secondary antibody for 1 h at RT. The immunoreactive bands were detected by ECL (Thermo Fisher Sci-entific) and recorded using XAR-5 film (Kodak).

RNA purification and real-time qPCR
RNA purification and cDNA synthesis were performed using TRIZOL re-agent (Invitrogen) and SuperScript II (Invitrogen), respectively, following the manufacturers' protocols. The qPCR was performed using the LightCycler FastStart DNA Master^{PLUS} SYBR green I kit with a LightCycler (Roche). PCRs were performed under the following conditions: 95°C for 10 min followed

by 40 cycles at 95°C for 10 s, 60°C for 5 s, and 72°C for 8 s. At least three different batches of cDNA and three independent PCRs were performed and were normalized to the expression of the reference gene glyceraldehyde-3-phosphate dehydrogenase (*Gapdh*). The primers used to amplify *Bcl2* and *Gapdh* were 5′-GAATGCAAAGCACATCCAATAAA-3′ and 5′-TCCAGCATCCCACTCGTA-3′ and 5′-TGACATCAAGAAGGTGGT-GAAG-3′ and 5′-AGAGTGGGAGTTGCTGTTGAAG-3′, respectively. The data were analyzed using RelQuant software (Roche).

Immunoprecipitation
Brain tissues were lysed with 1 ml of ice-cold RIPA buffer (0.1 M sodium phosphate, 10% sodium deoxycholate, 100% Triton X-100, and 5 M NaCl), incubated for 1 h at 4°C on a rolling wheel to dissolve the tissue, and were then incubated with an anti–AMPK-α1 or anti–AMPK-α2 antibody (Novus Biologicals) for 1 h at 4°C. The complexes were then mixed with protein A beads (Sigma-Aldrich) and incubated for another 1 h at 4°C. The immunocomplex was extensively washed with ice-cold RIPA buffer, solubilized in sample treatment buffer (62.5 mM Tris-HCl, pH 6.8, 10% glycerol, 2% SDS, and 0.01% bromophenol blue), and analyzed by SDS-PAGE and Western blot analysis.

Human brain tissue
5-μm brain sections of the human frontal cortex were obtained from the National Institute of Child Health and Human Development Brain and Tissue Bank for Developmental Disorders, and 5-μm brain sections of the caudate nucleus were obtained from the Mayo Clinic College of Medicine. The clinical characteristics of subjects are summarized in Table I. At least 200 cells were counted in brain sections of each subject.

Statistical analysis
The results are expressed as the mean ± SEM of triplicate samples. Each experiment was repeated at least three times to confirm the reproducibility of the findings. Multiple groups were analyzed with one-way analysis of variance followed by a posthoc Student Newman–Keuls test. A p-value of <0.05 was considered significant.

Online supplemental material
Fig. S1 shows selective activation and nuclear enrichment of AMPK-α1 in brains of patients and mice with HD. Fig. S2 shows that an inhibitor of AMPK, CC, reduced the nuclear enrichment of AMPK-α1 in the striatum of R6/2 mice. Fig. S3 shows nuclear enrichment of AMPK-α1 in striatal cells expressing polyQ-expanded mHtt. Fig. S4 shows that polyQ-expanded mHtt, but not SCA3, causes enrichment of AMPK-α1 in striatal cells. Fig. S5 shows that AMPK-α1 does not interact with the N-terminal fragment of Htt. Online supplemental material is available at http://www.jcb.org/cgi/content/full/jcb.201105010/DC1.

References

Anderson, K.A., T.J. Ribar, F. Lin, P.K. Noeldner, M.F. Green, M.J. Muehlbauer, L.A. Witters, B.E. Kemp, and A.R. Means. 2008. Hypothalamic CaMKK2 contributes to the regulation of energy balance. *Cell Metab.* 7:377–388. doi:10.1016/j.cmet.2008.02.011

Buckley, N.J., R. Johnson, C. Zuccato, A. Bithell, and E. Cattaneo. 2010. The role of REST in transcriptional and epigenetic dysregulation in Huntington's disease. *Neurobiol. Dis.* 39:28–39. doi:10.1016/j.nbd.2010.02.003

Cai, Y., G.A. Martens, S.A. Hinke, H. Heimberg, D. Pipeleers, and M. Van de Casteele. 2007. Increased oxygen radical formation and mitochondrial dysfunction mediate beta cell apoptosis under conditions of AMP-activated protein kinase stimulation. *Free Radic. Biol. Med.* 42:64–78. doi:10.1016/j.freeradbiomed.2006.09.018

Cattaneo, E., and L. Conti. 1998. Generation and characterization of embryonic striatal conditionally immortalized ST14A cells. *J. Neurosci. Res.* 53:223–234. doi:10.1002/(SICI)1097-4547(19980715)53:2<223::AID-JNR11>3.0.CO;2-7

Chai, Y., S.L. Koppenhafer, S.J. Shoesmith, M.K. Perez, and H.L. Paulson. 1999. Evidence for proteasome involvement in polyglutamine disease: localization to nuclear inclusions in SCA3/MJD and suppression of polyglutamine aggregation in vitro. *Hum. Mol. Genet.* 8:673–682. doi:10.1093/hmg/8.4.673

Chaturvedi, R.K., P. Adhihetty, S. Shukla, T. Hennessy, N. Calingasan, L. Yang, A. Starkov, M. Kiaei, M. Cannella, J. Sassone, et al. 2009. Impaired PGC-1alpha function in muscle in Huntington's disease. *Hum. Mol. Genet.* 18:3048–3065. doi:10.1093/hmg/ddp243

Chen, C.C., C.P. Sun, H.I. Ma, C.C. Fang, P.Y. Wu, X. Xiao, and M.H. Tao. 2009. Comparative study of anti-hepatitis B virus RNA interference by double-stranded adeno-associated virus serotypes 7, 8, and 9. *Mol. Ther.* 17:352–359. doi:10.1038/mt.2008.245

Chen, Y., K. Zhou, R. Wang, Y. Liu, Y.D. Kwak, T. Ma, R.C. Thompson, Y. Zhao, L. Smith, L. Gasparini, et al. 2009. Antidiabetic drug metformin (GlucophageR) increases biogenesis of Alzheimer's amyloid peptides via up-regulating BACE1 transcription. *Proc. Natl. Acad. Sci. USA.* 106:3907–3912. doi:10.1073/pnas.0807991106

Chern, Y., H.L. Lai, J.C. Fong, and Y. Liang. 1993. Multiple mechanisms for desensitization of A2a adenosine receptor-mediated cAMP elevation in rat pheochromocytoma PC12 cells. *Mol. Pharmacol.* 44:950–958.

Chiang, M.C., Y.C. Lee, C.L. Huang, and Y. Chern. 2005. cAMP-response element-binding protein contributes to suppression of the A2A adenosine receptor promoter by mutant Huntingtin with expanded polyglutamine residues. *J. Biol. Chem.* 280:14331–14340. doi:10.1074/jbc.M413279200

Chiang, M.C., H.M. Chen, Y.H. Lee, H.H. Chang, Y.C. Wu, B.W. Soong, C.M. Chen, Y.R. Wu, C.S. Liu, D.M. Niu, et al. 2007. Dysregulation of C/EBPalpha by mutant Huntingtin causes the urea cycle deficiency in Huntington's disease. *Hum. Mol. Genet.* 16:483–498. doi:10.1093/hmg/ddl481

Chou, S.Y., Y.C. Lee, H.M. Chen, M.C. Chiang, H.L. Lai, H.H. Chang, Y.C. Wu, C.N. Sun, C.L. Chien, Y.S. Lin, et al. 2005. CGS21680 attenuates symptoms of Huntington's disease in a transgenic mouse model. *J. Neurochem.* 93:310–320. doi:10.1111/j.1471-4159.2005.03029.x

Chou, S.Y., J.Y. Weng, H.L. Lai, F. Liao, S.H. Sun, P.H. Tu, D.W. Dickson, and Y. Chern. 2008. Expanded-polyglutamine huntingtin protein suppresses the secretion and production of a chemokine (CCL5/RANTES) by astrocytes. *J. Neurosci.* 28:3277–3290. doi:10.1523/JNEUROSCI.0116-08.2008

Cong, F., and H. Varmus. 2004. Nuclear-cytoplasmic shuttling of Axin regulates subcellular localization of beta-catenin. *Proc. Natl. Acad. Sci. USA.* 101:2882–2887. doi:10.1073/pnas.0307344101

Cui, L., H. Jeong, F. Borovecki, C.N. Parkhurst, N. Tanese, and D. Krainc. 2006. Transcriptional repression of PGC-1alpha by mutant huntingtin leads to mitochondrial dysfunction and neurodegeneration. *Cell.* 127:59–69. doi:10.1016/j.cell.2006.09.015

Escribano, C., C. Delgado-Martín, and J.L. Rodríguez-Fernández. 2009. CCR7-dependent stimulation of survival in dendritic cells involves inhibition of GSK3beta. *J. Immunol.* 183:6282–6295. doi:10.4049/jimmunol.0804093

Estrada Sánchez, A.M., J. Mejía-Toiber, and L. Massieu. 2008. Excitotoxic neuronal death and the pathogenesis of Huntington's disease. *Arch. Med. Res.* 39:265–276. doi:10.1016/j.arcmed.2007.11.011

Florant, G.L., A.M. Fenn, J.E. Healy, G.K. Wilkerson, and R.J. Handa. 2010. To eat or not to eat: the effect of AICAR on food intake regulation in yellow-bellied marmots (*Marmota flaviventris*). *J. Exp. Biol.* 213:2031–2037. doi:10.1242/jeb.039131

Fujii, N., T. Hayashi, M.F. Hirshman, J.T. Smith, S.A. Habinowski, L. Kaijser, J. Mu, O. Ljungqvist, M.J. Birnbaum, L.A. Witters, et al. 2000. Exercise induces isoform-specific increase in 5'AMP-activated protein kinase activity in human skeletal muscle. *Biochem. Biophys. Res. Commun.* 273:1150–1155. doi:10.1006/bbrc.2000.3073

Garcia-Gil, M., R. Pesi, S. Perna, S. Allegrini, M. Giannecchini, M. Camici, and M.G. Tozzi. 2003. 5′-aminoimidazole-4-carboxamide riboside induces apoptosis in human neuroblastoma cells. *Neuroscience.* 117:811–820. doi:10.1016/S0306-4522(02)00836-9

Giampà, C., S. Middei, S. Patassini, A. Borreca, F. Marullo, D. Laurenti, G. Bernardi, M. Ammassari-Teule, and F.R. Fusco. 2009. Phosphodiesterase type IV inhibition prevents sequestration of CREB binding protein, protects striatal parvalbumin interneurons and rescues motor defects in the R6/2 mouse model of Huntington's disease. *Eur. J. Neurosci.* 29:902–910. doi:10.1111/j.1460-9568.2009.06649.x

Greer, E.L., P.R. Oskoui, M.R. Banko, J.M. Maniar, M.P. Gygi, S.P. Gygi, and A. Brunet. 2007. The energy sensor AMP-activated protein kinase directly regulates the mammalian FOXO3 transcription factor. *J. Biol. Chem.* 282:30107–30119. doi:10.1074/jbc.M705325200

Hedbacker, K., and M. Carlson. 2006. Regulation of the nucleocytoplasmic distribution of Snf1-Gal83 protein kinase. *Eukaryot. Cell.* 5:1950–1956. doi:10.1128/EC.00256-06

Horike, N., H. Sakoda, A. Kushiyama, H. Ono, M. Fujishiro, H. Kamata, K. Nishiyama, Y. Uchijima, Y. Kurihara, H. Kurihara, and T. Asano. 2008. AMP-activated protein kinase activation increases phosphorylation of glycogen synthase kinase 3beta and thereby reduces cAMP-responsive element transcriptional activity and phosphoenolpyruvate carboxykinase C gene expression in the liver. *J. Biol. Chem.* 283:33902–33910. doi:10.1074/jbc.M802537200

Hurlbert, M.S., W. Zhou, C. Wasmeier, F.G. Kaddis, J.C. Hutton, and C.R. Freed. 1999. Mice transgenic for an expanded CAG repeat in the Huntington's disease gene develop diabetes. *Diabetes.* 48:649–651. doi:10.2337/diabetes.48.3.649

Hurley, R.L., L.K. Barré, S.D. Wood, K.A. Anderson, B.E. Kemp, A.R. Means, and L.A. Witters. 2006. Regulation of AMP-activated protein kinase by multisite phosphorylation in response to agents that elevate cellular cAMP. *J. Biol. Chem.* 281:36662–36672. doi:10.1074/jbc.M606676200

Jäger, S., C. Handschin, J. St-Pierre, and B.M. Spiegelman. 2007. AMP-activated protein kinase (AMPK) action in skeletal muscle via direct phosphorylation of PGC-1alpha. *Proc. Natl. Acad. Sci. USA.* 104:12017–12022. doi:10.1073/pnas.0705070104

Ju, T.C., S.D. Chen, C.C. Liu, and D.I. Yang. 2005. Protective effects of S-nitrosoglutathione against amyloid beta-peptide neurotoxicity. *Free Radic. Biol. Med.* 38:938–949. doi:10.1016/j.freeradbiomed.2004.12.019

Jung, J.E., J. Lee, J. Ha, S.S. Kim, Y.H. Cho, H.H. Baik, and I. Kang. 2004. 5-Aminoimidazole-4-carboxamide-ribonucleoside enhances oxidative stress-induced apoptosis through activation of nuclear factor-kappaB in mouse Neuro 2a neuroblastoma cells. *Neurosci. Lett.* 354:197–200. doi:10.1016/j.neulet.2003.10.012

Kefas, B.A., Y. Cai, Z. Ling, H. Heimberg, L. Hue, D. Pipeleers, and M. Van de Casteele. 2003. AMP-activated protein kinase can induce apoptosis of insulin-producing MIN6 cells through stimulation of c-Jun-N-terminal kinase. *J. Mol. Endocrinol.* 30:151–161. doi:10.1677/jme.0.0300151

Kodiha, M., J.G. Rassi, C.M. Brown, and U. Stochaj. 2007. Localization of AMP kinase is regulated by stress, cell density, and signaling through the MEK—>ERK1/2 pathway. *Am. J. Physiol. Cell Physiol.* 293:C1427–C1436. doi:10.1152/ajpcell.00176.2007

Landles, C., and G.P. Bates. 2004. Huntingtin and the molecular pathogenesis of Huntington's disease. Fourth in molecular medicine review series. *EMBO Rep.* 5:958–963. doi:10.1038/sj.embor.7400250

Lee, M.J., C.P. Chang, Y.H. Lee, Y.C. Wu, H.W. Tseng, Y.Y. Tung, M.T. Wu, Y.H. Chen, L.T. Kuo, D. Stephenson, et al. 2009. Longitudinal evaluation of an N-ethyl-N-nitrosourea-created murine model with normal pressure hydrocephalus. *PLoS ONE.* 4:e7868. doi:10.1371/journal.pone.0007868

Liu, F.C., G.C. Wu, S.T. Hsieh, H.L. Lai, H.F. Wang, T.W. Wang, and Y. Chern. 1998. Expression of type VI adenylyl cyclase in the central nervous system: implication for a potential regulator of multiple signals in different neurotransmitter systems. *FEBS Lett.* 436:92–98. doi:10.1016/S0014-5793(98)01098-9

Long, Y.C., and J.R. Zierath. 2006. AMP-activated protein kinase signaling in metabolic regulation. *J. Clin. Invest.* 116:1776–1783. doi:10.1172/JCI29044

Lopez-Lopez, C., M.O. Dietrich, F. Metzger, H. Loetscher, and I. Torres-Aleman. 2007. Disturbed cross talk between insulin-like growth factor I and AMP-activated protein kinase as a possible cause of vascular dysfunction in the amyloid precursor protein/presenilin 2 mouse model of Alzheimer's disease. *J. Neurosci.* 27:824–831. doi:10.1523/JNEUROSCI.4345-06.2007

Ma, T.C., J.L. Buescher, B. Oatis, J.A. Funk, A.J. Nash, R.L. Carrier, and K.R. Hoyt. 2007. Metformin therapy in a transgenic mouse model of Huntington's disease. *Neurosci. Lett.* 411:98–103. doi:10.1016/j.neulet.2006.10.039

Mangiarini, L., K. Sathasivam, M. Seller, B. Cozens, A. Harper, C. Hetherington, M. Lawton, Y. Trottier, H. Lehrach, S.W. Davies, and G.P. Bates. 1996. Exon 1 of the HD gene with an expanded CAG repeat is sufficient to cause a progressive neurological phenotype in transgenic mice. *Cell.* 87:493–506. doi:10.1016/S0092-8674(00)81369-0

Martin, J.B., and J.F. Gusella. 1986. Huntington's disease. Pathogenesis and management. *N. Engl. J. Med.* 315:1267–1276. doi:10.1056/NEJM198611133152006

McCullough, L.D., Z. Zeng, H. Li, L.E. Landree, J. McFadden, and G.V. Ronnett. 2005. Pharmacological inhibition of AMP-activated protein kinase provides neuroprotection in stroke. *J. Biol. Chem.* 280:20493–20502. doi:10.1074/jbc.M409985200

Meisse, D., M. Van de Casteele, C. Beauloye, I. Hainault, B.A. Kefas, M.H. Rider, F. Foufelle, and L. Hue. 2002. Sustained activation of AMP-activated protein kinase induces c-Jun N-terminal kinase activation and apoptosis in liver cells. *FEBS Lett.* 526:38–42. doi:10.1016/S0014-5793(02)03110-1

Musi, N., N. Fujii, M.F. Hirshman, I. Ekberg, S. Fröberg, O. Ljungqvist, A. Thorell, and L.J. Goodyear. 2001. AMP-activated protein kinase (AMPK) is activated in muscle of subjects with type 2 diabetes during exercise. *Diabetes.* 50:921–927. doi:10.2337/diabetes.50.5.921

Nicoletti, I., G. Migliorati, M.C. Pagliacci, F. Grignani, and C. Riccardi. 1991. A rapid and simple method for measuring thymocyte apoptosis by propidium iodide staining and flow cytometry. *J. Immunol. Methods.* 139:271–279. doi:10.1016/0022-1759(91)90198-O

Okoshi, R., T. Ozaki, H. Yamamoto, K. Ando, N. Koida, S. Ono, T. Koda, T. Kamijo, A. Nakagawara, and H. Kizaki. 2008. Activation of AMP-activated protein kinase induces p53-dependent apoptotic cell death in response to energetic stress. *J. Biol. Chem.* 283:3979–3987. doi:10.1074/jbc.M705232200

Pan, T., M. Cai, L. Tang, L.Q. Zhou, B.J. Li, T. Zhu, H.Z. Li, S.Y. Li, X. Xiao, and Z.S. Chen. 2008. A novel approach of prophylaxis to HBV recurrence after liver transplantation. *Virology.* 382:1–9. doi:10.1016/j.virol.2008.06.024

Parker, D., K. Ferreri, T. Nakajima, V.J. LaMorte, R. Evans, S.C. Koerber, C. Hoeger, and M.R. Montminy. 1996. Phosphorylation of CREB at Ser-133 induces complex formation with CREB-binding protein via a direct mechanism. *Mol. Cell. Biol.* 16:694–703.

Pratley, R.E., A.D. Salbe, E. Ravussin, and J.N. Caviness. 2000. Higher sedentary energy expenditure in patients with Huntington's disease. *Ann. Neurol.* 47:64–70. doi:10.1002/1531-8249(200001)47:1<64::AID-ANA11>3.0.CO;2-S

Raney, M.A., and L.P. Turcotte. 2008. Evidence for the involvement of CaMKII and AMPK in Ca2+-dependent signaling pathways regulating FA uptake and oxidation in contracting rodent muscle. *J. Appl. Physiol.* 104:1366–1373. doi:10.1152/japplphysiol.01282.2007

Riol-Blanco, L., C. Delgado-Martín, N. Sánchez-Sánchez, L.M. Alonso-C, M.D. Gutiérrez-López, G.M. Del Hoyo, J. Navarro, F. Sánchez-Madrid, C. Cabañas, P. Sánchez-Mateos, and J.L. Rodríguez-Fernández. 2009. Immunological synapse formation inhibits, via NF-kappaB and FOXO1, the apoptosis of dendritic cells. *Nat. Immunol.* 10:753–760. doi:10.1038/ni.1750

Salt, I., J.W. Celler, S.A. Hawley, A. Prescott, A. Woods, D. Carling, and D.G. Hardie. 1998. AMP-activated protein kinase: greater AMP dependence, and preferential nuclear localization, of complexes containing the alpha2 isoform. *Biochem. J.* 334:177–187.

Shaw, M.M., W.K. Gurr, R.J. McCrimmon, D.F. Schorderet, and R.S. Sherwin. 2007. 5'AMP-activated protein kinase alpha deficiency enhances stress-induced apoptosis in BHK and PC12 cells. *J. Cell. Mol. Med.* 11:286–298. doi:10.1111/j.1582-4934.2007.00023.x

Stapleton, D., K.I. Mitchelhill, G. Gao, J. Widmer, B.J. Michell, T. Teh, C.M. House, C.S. Fernandez, T. Cox, L.A. Witters, and B.E. Kemp. 1996. Mammalian AMP-activated protein kinase subfamily. *J. Biol. Chem.* 271:611–614. doi:10.1074/jbc.271.45.28445

Stein, S.C., A. Woods, N.A. Jones, M.D. Davison, and D. Carling. 2000. The regulation of AMP-activated protein kinase by phosphorylation. *Biochem. J.* 345:437–443. doi:10.1042/0264-6021:3450437

Swulius, M.T., and M.N. Waxham. 2008. Ca(2+)/calmodulin-dependent protein kinases. *Cell. Mol. Life Sci.* 65:2637–2657. doi:10.1007/s00018-008-8086-2

Tang, T.S., E. Slow, V. Lupu, I.G. Stavrovskaya, M. Sugimori, R. Llinás, B.S. Kristal, M.R. Hayden, and I. Bezprozvanny. 2005. Disturbed Ca2+ signaling and apoptosis of medium spiny neurons in Huntington's disease. *Proc. Natl. Acad. Sci. USA.* 102:2602–2607. doi:10.1073/pnas.0409402102

The Huntington's Disease Collaborative Research Group. 1993. A novel gene containing a trinucleotide repeat that is expanded and unstable on Huntington's disease chromosomes. *Cell.* 72:971–983. doi:10.1016/0092-8674(93)90585-E

Tsuboi, T., G. da Silva Xavier, I. Leclerc, and G.A. Rutter. 2003. 5′-AMP-activated protein kinase controls insulin-containing secretory vesicle dynamics. *J. Biol. Chem.* 278:52042–52051. doi:10.1074/jbc.M307800200

Turnley, A.M., D. Stapleton, R.J. Mann, L.A. Witters, B.E. Kemp, and P.F. Bartlett. 1999. Cellular distribution and developmental expression of AMP-activated protein kinase isoforms in mouse central nervous system. *J. Neurochem.* 72:1707–1716. doi:10.1046/j.1471-4159.1999.721707.x

Valenza, M., J.B. Carroll, V. Leoni, L.N. Bertram, I. Björkhem, R.R. Singaraja, S. Di Donato, D. Lutjohann, M.R. Hayden, and E. Cattaneo. 2007. Cholesterol biosynthesis pathway is disturbed in YAC128 mice and is modulated by huntingtin mutation. *Hum. Mol. Genet.* 16:2187–2198. doi:10.1093/hmg/ddm170

Warden, S.M., C. Richardson, J. O'Donnell Jr., D. Stapleton, B.E. Kemp, and L.A. Witters. 2001. Post-translational modifications of the beta-1 subunit of AMP-activated protein kinase affect enzyme activity and cellular localization. *Biochem. J.* 354:275–283. doi:10.1042/0264-6021:3540275

Weekes, J., K.L. Ball, F.B. Caudwell, and D.G. Hardie. 1993. Specificity determinants for the AMP-activated protein kinase and its plant homologue analysed using synthetic peptides. *FEBS Lett.* 334:335–339. doi:10.1016/0014-5793(93)80706-Z

Wojtaszewski, J.F., J.B. Birk, C. Frøsig, M. Holten, H. Pilegaard, and F. Dela. 2005. 5'AMP activated protein kinase expression in human skeletal muscle: effects of strength training and type 2 diabetes. *J. Physiol.* 564:563–573. doi:10.1113/jphysiol.2005.082669

Woods, A., I. Salt, J. Scott, D.G. Hardie, and D. Carling. 1996. The alpha1 and alpha2 isoforms of the AMP-activated protein kinase have similar activities in rat liver but exhibit differences in substrate specificity in vitro. *FEBS Lett.* 397:347–351. doi:10.1016/S0014-5793(96)01209-4

Xiao, X., J. Li, and R.J. Samulski. 1998. Production of high-titer recombinant adeno-associated virus vectors in the absence of helper adenovirus. *J. Virol.* 72:2224–2232.

Yang, W., Y.H. Hong, X.Q. Shen, C. Frankowski, H.S. Camp, and T. Leff. 2001. Regulation of transcription by AMP-activated protein kinase: phosphorylation of p300 blocks its interaction with nuclear receptors. *J. Biol. Chem.* 276:38341–38344. doi:10.1074/jbc.C100316200

Zang, Y., L.F. Yu, T. Pang, L.P. Fang, X. Feng, T.Q. Wen, F.J. Nan, L.Y. Feng, and J. Li. 2008. AICAR induces astroglial differentiation of neural stem cells via activating the JAK/STAT3 pathway independently of AMP-activated protein kinase. *J. Biol. Chem.* 283:6201–6208. doi:10.1074/jbc.M708619200

Zhang, Y., V.O. Ona, M. Li, M. Drozda, M. Dubois-Dauphin, S. Przedborski, R.J. Ferrante, and R.M. Friedlander. 2003. Sequential activation of individual caspases, and of alterations in Bcl-2 proapoptotic signals in a mouse model of Huntington's disease. *J. Neurochem.* 87:1184–1192. doi:10.1046/j.1471-4159.2003.02105.x